

## Gulf Stream Dynamics along the Southeastern U.S. Seaboard

JONATHAN GULA, M. JEROEN MOLEMAKER, AND JAMES C. MCWILLIAMS

*Department of Atmospheric and Oceanic Sciences, University of California, Los Angeles, Los Angeles, California*

(Manuscript received 30 July 2014, in final form 4 December 2014)

### ABSTRACT

The Gulf Stream strongly interacts with the topography along the southeastern U.S. seaboard, between the Straits of Florida and Cape Hatteras. The dynamics of the Gulf Stream in this region is investigated with a set of realistic, very high-resolution simulations using the Regional Ocean Modeling System (ROMS). The mean path is strongly influenced by the topography and in particular the Charleston Bump. There are significant local pressure anomalies and topographic form stresses exerted by the bump that retard the mean flow and steer the mean current pathway seaward. The topography provides, through bottom pressure torque, the positive input of barotropic vorticity necessary to balance the meridional transport of fluid and close the gyre-scale vorticity balance. The effect of the topography on the development of meanders and eddies is studied by computing energy budgets of the eddies and the mean flow. The baroclinic instability is stabilized by the slope everywhere except past the bump. The flow is barotropically unstable, and kinetic energy is converted from the mean flow to the eddies following the Straits of Florida and at the bump with regions of eddy-to-mean conversion in between. There is eddy growth by Reynolds stress and downstream development of the eddies. Interaction of the flow with the topography acts as an external forcing process to localize these oceanic storm tracks. Associated time-averaged eddy fluxes are essential to maintain and reshape the mean current. The pattern of eddy fluxes is interpreted in terms of eddy life cycle, eddy fluxes being directed downgradient in eddy growth regions and upgradient in eddy decay regions.

### 1. Introduction

The Gulf Stream is fed by the Loop Current in the Gulf of Mexico and the Antilles Current. It passes through the Strait of Florida and then flows northward pressed against the confining wall of the southeastern U.S. continental shelf, also known as the South Atlantic Bight, before leaving the slope at Cape Hatteras. The mean path of the stream along the coast is controlled by a combination of boundary shape, bottom topography, entrainment of fluid from the gyre interior, and the adjustment of the flow to the increase in planetary vorticity as fluid is advected northward (Olson et al. 1983). Eddies also provide important material and dynamical fluxes for the maintenance of the Gulf Stream (McWilliams 2008).

An example of satellite observed sea surface temperature (SST) of the Gulf Stream in this region is in

**Fig. 1.** Meanders and eddies are common features of the Gulf Stream between the Straits of Florida and Cape Hatteras. Large meanders are visible on the inshore side of the Gulf Stream, with cyclonic eddies propagating along the shelf. These eddies are referred to as “frontal eddies” and occur where the Gulf Stream interacts with the slope and shelf (see, e.g., Glenn and Ebbesmeyer 1994, and references therein). They are formed in the troughs of northward-propagating meanders and consist of deep, upwelled, cold domes. They are often associated with shallow, warm filaments, known as “shingles” (von Arx et al. 1955), which form at the surface and extend from the leading meander crest along the shoreward side of the cold dome.

Eddies and meanders have strong implications for the biological production in the South Atlantic Bight (Lee et al. 1991). The upwelling pumps nutrient-rich bottom waters toward the surface, resulting in high levels of ocean productivity. Elevated nutrients, phytoplankton blooms, and trophic transfers to zooplankton are observed within eddies (McClain and Atkinson 1985). Eddies also induce cross-shelf exchange processes with the adjacent shelf water with important dynamical, ecological, and water

*Corresponding author address:* Jonathan Gula, Department of Atmospheric and Oceanic Sciences, University of California, Los Angeles, 405 Hilgard Ave., Los Angeles, CA 90095-1565.  
E-mail: gula@atmos.ucla.edu

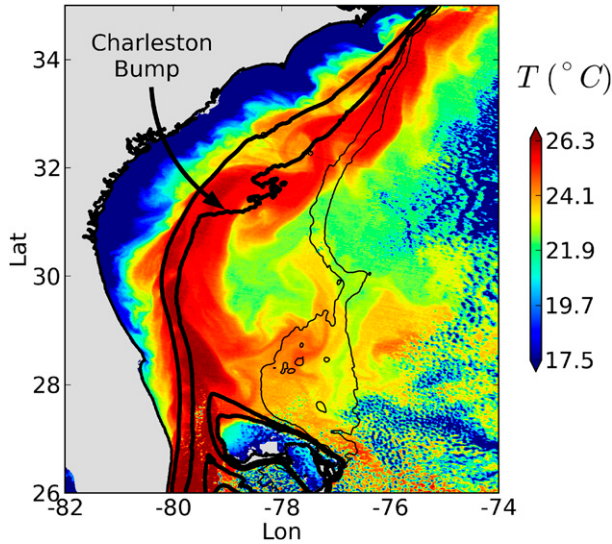


FIG. 1. Observed SST of the Gulf Stream on 23 Dec 2012. Data from MODIS–Aqua. Topography is shown in black contours at 0-, 200-, 600-, 1000-, and 2000-m isobaths. The hot Gulf Stream is deflected eastward at the Charleston Bump location. Large meanders form downstream of the bump with frontal eddies in between detraining water from the crests to form the so-called shingles patterns. Frontal eddies have decreasing size as they are approaching Cape Hatteras.

quality implications (Blanton et al. 1981; Lee and Atkinson 1983; McClain et al. 1984; Yoder et al. 1985; Lee et al. 1991).

#### a. Charleston Bump

The  $z = -600$ -m isobath in Fig. 1 highlights a prominent topographic feature centered at  $31.5^{\circ}\text{N}$ ,  $79^{\circ}\text{W}$  off the coast of South Carolina and Georgia. This feature, called the Charleston Bump, rises off the surrounding Blake Plateau from 600 m deep to a depth of about 200 m. A more detailed view of the topography of the region is shown in Fig. 2. The Charleston Bump is only a small feature on bathymetric maps, and the associated topographic gradients are small compared to the Blake Escarpment or the continental shelf upstream. However, its location right under the path of the Gulf Stream makes its influence on the current particularly strong. Just after the Gulf Stream begins bending to the east, following the curve of the continental shelf, it runs directly over the Charleston Bump. When the Gulf Stream encounters the Charleston Bump, it is suddenly disrupted. The direction of the flow deflects farther eastward, and large meanders are generated, as seen on satellite images of SST in Fig. 1. This deflection of the flow results in a quasi-stationary cyclonic eddy referred to as the Charleston Gyre (McClain and Atkinson 1985). The Gulf Stream position downstream of the Charleston Bump is described

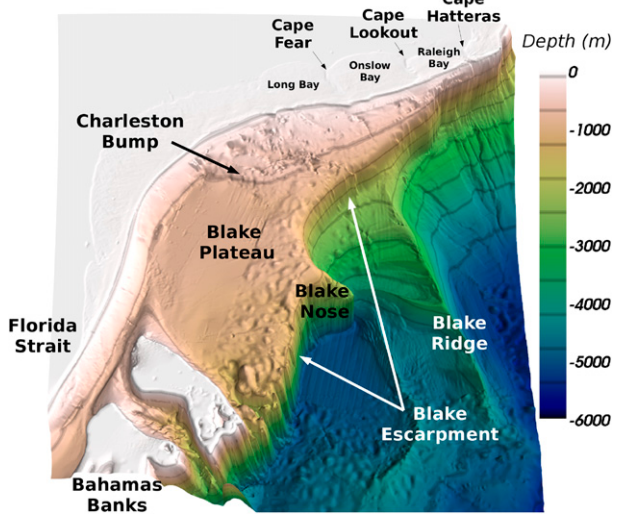


FIG. 2. Topography (m) of the South Atlantic Bight from the SRTM30\_PLUS dataset. The Charleston Bump lies at the north end of the Blake Plateau. The topography has been interpolated on the grid of the ROMS2 simulation ( $\Delta x = 750$  m; see section 2).

by Bane and Dewar (1988) as having a bimodal character with a weakly deflected state, where the shoreward Gulf Stream front remains inshore of the 600-m isobath, and a strongly deflected state, where the front is located offshore of the 600-m isobath, forming the Charleston Gyre.

The degree to which the Charleston Bump affects the Gulf Stream path and velocity is, however, still not fully understood. The pressure forces at the bump generate drags and torques likely to impact strongly the momentum and vorticity balances of the stream and which remain to be quantified.

#### b. Observed Gulf Stream variability

The role of the topography, and in particular the bump, is not simply to steer the flow but is expected to have a broader indirect dynamical influence. Observations link the variability of the stream to the characteristics of the topography.

The Charleston Bump has been identified as a preferred region for eddy generation using satellite-based measurements and statistics. Satellite observations show a steady increase of the variance of the stream position between the Florida Straits and Charleston Bump, followed by a sharp increase downstream of the bump and a gradual decay from approximately  $33^{\circ}\text{N}$  to Cape Hatteras (Olson et al. 1983). This has led to the “amplification hypothesis,” described in Hood and Bane (1983) and Dewar and Bane (1985), with different sections of the shelf acting either as amplification or dissipation regions for the eddies. Energy conversions from barotropic and baroclinic instabilities observed in the

Gulf Stream seem to be independent from each other, with the former being larger than the latter ([Dewar and Bane 1985](#)). It was noted first by [Webster \(1961\)](#), who calculated the transfer of kinetic energy between the mean flow and the meanders near Miami (26°N) and off Onslow Bay (33.5°N), that the energy conversion is from the eddies to the mean flow at the two locations, with maximum values measured in regions of high cyclonic shear. Subsurface measurements off Onslow Bay by [Hood and Bane \(1983\)](#) confirm the eddy-to-mean energy conversion and characterize the region as a region of decreasing meander amplitude. The more complete energy budgets of the eddy and mean flow upstream and downstream of the Charleston Bump presented in [Hood and Bane \(1983\)](#) and [Dewar and Bane \(1985\)](#) show both a large mean-to-eddy conversion at the bump and eddy-to-mean conversion downstream. Results from different studies using satellite imagery and moored current and temperature records are reviewed by [Lee et al. \(1991\)](#). They describe a first amplification region north of the Florida Strait between 27° and 30°N and a second one downstream of the Charleston Bump between 32° and 33°N, with mostly eddy energy decay in regions in between.

There is a mean-to-eddy energy conversion where the mean velocity gradient is the source for eddy generation through instability processes. This implies a down-gradient momentum transport and a deceleration of the mean flow. The eddy-to-mean conversion energy on the other hand is somehow counterintuitive as it requires an upgradient momentum transport. The eddies are accelerating the mean flow, in effect corresponding to a negative eddy viscosity. [Webster \(1961\)](#), [Dewar and Bane \(1985\)](#), and [Lin and Atkinson \(2000\)](#) show that the elongated eddies observed in this region can create such upgradient momentum transport depending on the orientation of their major axis relative to the mean shear direction on the cyclonic side of the stream.

According to [Lee et al. \(1991\)](#), the eddy decay regions are mostly associated with offshore transport of momentum and heat and onshore transport of nutrients. These results are difficult to confirm, and the observed fluxes are sometimes contradictory because of the sparsity of the in situ data and the difficulty sampling adequately such highly variable turbulent fluxes.

### c. Gulf Stream stability along the seaboard

An important issue is to understand the mechanisms controlling eddy generation and decay in the presence of topography.

Multiple idealized studies of the Gulf Stream stability along the shelf have been performed in the past. [Orlanski \(1969\)](#) studies the stability of a two-layer model with

bottom topography and finds that the topographic slope has a stabilizing effect for baroclinic instability. [Xue and Mellor \(1993\)](#) extend the linear stability analysis using linearized primitive equations with analytical profiles for the cross-frontal slope, representing the mean profiles upstream and downstream of the bump. They find that the long-wave baroclinic instability is the most unstable mode on the shoreward side and predict longer wavelength and slower phase speed downstream of the bump than in the region upstream because of the different characteristics of the slope.

Linear stability analysis shows that a shelf slope always has a stabilizing effect for the baroclinic instability of retrograde current such as the Gulf Stream ([Pennel et al. 2012](#); [Gula and Zeitlin 2014](#)). A coastal flow is retrograde if the topographic Rossby waves propagate in the opposite direction from the current, meaning that the flow has the coast on its left in the Northern Hemisphere. This corresponds to a positive ratio of the bottom slope over the isopycnal slope. There is, however, no direct and simple effect of the slope on the linear stability for barotropic-type mechanisms of a baroclinic flow (e.g., [Poulin et al. 2014](#)).

Linear stability analysis cannot predict the final amplitude of unstable meanders, and it has been shown that the bottom topography can have a strong impact on the nonlinear saturation of the instability processes. In particular, surface meanders generate deep eddies that can provide a feedback on the meander growth ([Savidge and Bane 1999](#)).

An example of a simplified model for nonlinear evolution of meanders and frontal instabilities in the Gulf Stream is presented in [Oey \(1988\)](#). It shows that the growth of finite-amplitude disturbances is dependent on the cross-stream distance between the slope, in their case a vertical wall, and the Gulf Stream front. A large review on the stability of Gulf Stream meanders along the U.S. seaboard is provided in [Miller and Lee \(1995\)](#). They also analyze the energetics of idealized numerical simulations using the Princeton Ocean Model and conclude that mixed barotropic–baroclinic instability processes are responsible for the meander growth.

Another characteristic of the bathymetry of the shelf is the curvature of the isobaths. As noted by [Xie et al. \(2007\)](#), the isobaths are north–south oriented south of 30°N and turn sharply to northeast–southwest around 31°N. The Charleston Bump is located in a region where the curvature of the isobaths is very large. Simulations using idealized topography performed by [Xie et al. \(2007\)](#) show that both the isobathic curvature and the bump play a role in the instability of the current. They conclude that the curvature plays a role in enhancing the baroclinic and barotropic energy conversion, whereas

the bump provides a local mechanism to maximize the energy transfer rate.

In the present study, we investigate the dynamics of the Gulf Stream along the seaboard with a set of realistic, very high-resolution simulations. Our goal in this study is to understand and quantify the role played by the interactions of the flow with topographic features, and the subsequent impact of nonlinear eddy-mean flow interactions, to set the characteristics of the stream. Observations do not give a complete picture of the dynamics because of the limitations in instrumental sampling. Theoretical studies and idealized simulations give very valuable insights on different aspects of the dynamics but do not yet fully explain the observed characteristics of the flow. A realistic model can provide the high spatial and temporal resolution information required for characterization of the relevant dynamical processes.

The paper is organized as follows: The simulation setup is presented in section 2. Characteristics of the mean Gulf Stream in the simulations are described and compared to observations in section 3. In section 4, the topographic influence on the flow is analyzed through diagnostics of bottom pressure anomaly, form drag, and bottom pressure torque. The eddy-mean interactions are analyzed in section 5. Conclusions are presented and discussed in section 6.

## 2. Model setup

In the following, we present realistic simulations of the Gulf Stream region, realized with the Regional Oceanic Modeling System (ROMS; Shchepetkin and McWilliams 2005). It solves the hydrostatic primitive equations for the velocity  $\mathbf{u}$ , temperature  $T$ , and salinity  $S$ , using a full equation of state for seawater (Shchepetkin and McWilliams 2008, 2011). We use a nesting approach with successive horizontal grid nesting refinements from a parent grid resolution of  $\Delta x \approx 6$  km covering most of the Atlantic Ocean to successive child grids with  $\Delta x \approx 2.5$  km and  $\Delta x \approx 750$  m. These successive domains are shown in Fig. 3.

The nesting procedure is one way, from larger to finer scales without feedback from the child grid solution onto the parent grid (Penven et al. 2006), and offline, grids are run independently and each nest supplies boundary forcing data to the next one. The boundary condition algorithm consists of a modified Flather-type scheme for the barotropic mode (Mason et al. 2010) and an Orlanski-type scheme for the baroclinic mode (including  $T$  and  $S$ ; Marchesiello et al. 2001).

Bathymetry for all domains is constructed from the SRTM30\_PLUS dataset (available online at [http://topex.ucsd.edu/WWW\\_html/srtm30\\_plus.html](http://topex.ucsd.edu/WWW_html/srtm30_plus.html)) based

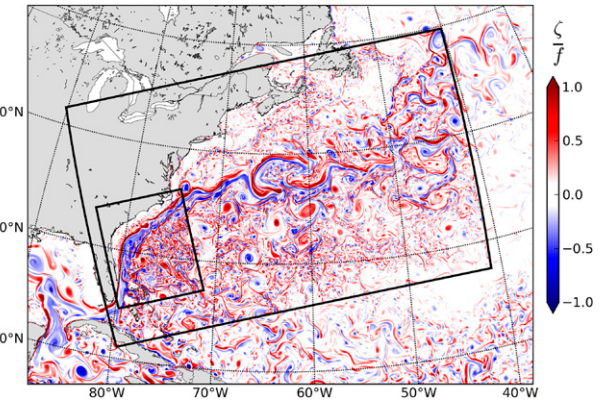


FIG. 3. Instantaneous surface relative vorticity  $\zeta = v_x - u_y$  in the region of the Gulf Stream at the end of winter as simulated by ROMS. The parent domain ROMS0 ( $\Delta x \approx 6$  km) covers most of the Atlantic Ocean (not shown). The boundaries of the successive nested domains ROMS1 ( $\Delta x = 2.5$  km) and ROMS2 ( $\Delta x = 750$  m) are delineated by thick black lines. The relative vorticity plotted inside each of the domains is computed using data at the corresponding resolution. The successive levels of grid refinement spontaneously exhibit an increasingly realistic amount of submesoscale activity.

on the 1-min Smith and Sandwell (1997) global dataset and higher-resolution data where available. A Gaussian smoothing kernel with a width of 4 times the topographic grid spacing is used to avoid aliasing whenever the topographic data are available at higher resolution than the computational grid. Terrain-following models such as ROMS have computational restrictions with regards to the steepness and roughness of the topography (Beckmann and Haidvogel 1993). Local smoothing is applied where the steepness of the topography exceeds a factor  $r_{\max} = 0.2$ .

Lateral oceanic forcings for the largest domain and surface forcings for all simulations are climatological. Simulations are all forced at the surface by high-frequency winds constructed from a climatology of QuikSCAT scatterometer winds [Scatterometer Climatology of Ocean Wind (SCOW); Risien and Chelton 2008] with the addition of daily winds that have the right amount of climatological variance following the methodology described in Lemarié et al. (2012). Heat and freshwater atmospheric forcing are from COADS (Silva et al. 1994). Freshwater atmospheric forcing has an additional restoring tendency to prevent surface salinity from drifting away from climatological values. This weak restoring is toward climatological monthly surface salinity from the *World Ocean Atlas* (WOA; Conkright et al. 2002). A flux correction term is included in heat atmospheric forcing to allow feedback from the ocean to the atmosphere, following the formulation of Barnier et al. (1995). Temperature, salinity, surface elevation, and horizontal velocity initial and boundary

information for the largest domain covering the Atlantic Ocean are taken from the monthly averaged SODA ocean climatology outputs ([Carton and Giese 2008](#)).

The Atlantic domain, hereinafter ROMS0, is a  $2000 \times 1500$  point orthogonal grid based on an oblique Mercator projection and designed to have nearly uniform spacing in both horizontal directions. This domain is spun up from its initial state for 2 yr. Once equilibrated, we use one full year of the solution, at 5-day intervals, to provide data at the open boundaries of a nested grid covering the whole Gulf Stream region (ROMS1;  $1600 \times 1000$  grid points with  $\Delta x \approx 2.5$  km). The boundary data from the ROMS0 solution are repeated for 18 yr to get a statistically significant sample of internal variability in the nested domain. Results from this first nest are used to force a 1-yr-long simulation over a second nest (ROMS2;  $1200 \times 1400$  grid points with  $\Delta x \approx 750$  m) covering the South Atlantic Bight, between Cape Canaveral and Cape Hatteras. The second nest allows us to investigate the interaction of the Gulf Stream with the continental shelf and in particular the Charleston Bump in more detail. All domains have 50 levels in the vertical with the same vertical grid system concentrating vertical levels near the surface and bottom following the formula described in [Lemarié et al. \(2012\)](#). The depth of the transition between flat  $z$  levels and terrain-following  $\sigma$  levels is  $h_{\text{cline}} = 300$  m. The two parameters controlling the bottom and surface refinement of the grid are  $\theta_b = 2$ , and  $\theta_s = 7$ , respectively. Vertical mixing of tracers and momentum is done with a  $K$ -profile parameterization (KPP; [Large et al. 1994](#)) at the surface and bottom, with the modifications described in [Lemarié et al. \(2012\)](#) based on a bulk Richardson number critical value, here  $Ri_{\text{cr}} = 0.15$ . Following recommendations of [McWilliams et al. \(2009\)](#), the value of the Richardson number has been decreased compared to the otherwise similar simulations presented in [Gula et al. \(2014\)](#), where a value of  $Ri_{\text{cr}} = 0.45$  was used because of the addition of a diurnal cycle in the formulation of the surface buoyancy forcing in the present simulation. The effect of bottom friction is parameterized through a logarithmic law of the wall with a roughness length  $Z_0 = 0.01$  m.

### 3. Gulf Stream structure

We describe in this section the characteristics of the Gulf Stream along the southeast continental shelf in the simulations and compare them to available satellite and in situ observations. Characteristics of the mean Gulf Stream include the location of its path, the horizontal and vertical structure of the velocity amplitude and velocity shear, the total transport, and the stratification of the flow. We also address the variability of the Gulf Stream position at the bump by investigating the path

position bimodality at the bump and comparing the eddy variability in the model to altimetric observations.

#### a. Characteristics of the mean Gulf Stream

The mean sea surface height  $\eta$  and the corresponding geostrophic current ( $g|\nabla\eta|/f$ , where  $g$  is the gravitational acceleration and  $f$  the Coriolis frequency) from 18 yr of ROMS1 are shown in [Fig. 4](#), along with observations from the  $1/4^\circ$  resolution CNES-CLS09 dataset, which is a combination of GRACE data, altimetry, and in situ measurements ([Rio et al. 2011](#)). The spatial distribution and amplitude of the simulated  $\eta$  compare well to the observations. The mean path of the Gulf Stream, in particular, is very well matched. It follows closely the  $z = -200$ -m isobath between the Straits of Florida and the Charleston Bump, is strongly deflected seaward when flowing over the bump, and slowly recovers between the bump and Cape Lookout. [Figure 4e](#) shows the exact location of the maximum velocity value and the maximum and minimum values of the cross-stream velocity shear relative to the 200-m isobath for both ROMS1 and observations. The main difference between model and observations is the slightly smaller deflection, which is likely a consequence of a weaker transport in the model than in observations.

The spatial distribution of the geostrophic current, derived from simulated and observed sea surface height, is in very good agreement. The maximum amplitude of the current is, however, slightly stronger in the model than in the observations. The CNES-CLS09 dataset is able to resolve much stronger gradients for western boundary currents, and in particular the Gulf Stream, than other comparable datasets ([Rio et al. 2011](#)). But, as can be expected from the coarse temporal (1 week) and spatial (100 km) resolution of the altimetric observations, altimetric geostrophic velocity amplitudes are usually too weak compared to in situ geostrophic velocities. Statistical comparisons of the CNES-CLS09 dataset with independent in situ velocities were performed by [Rio et al. \(2011\)](#) who computed a mean regression slope  $\approx 0.7$  in the Gulf Stream region. If we compare velocities in the core of the Gulf Stream, we get mean factors 0.94, 0.87, and 0.83 between the amplitude of the velocities from the CNES-CLS09 dataset and those from the ROMS0, ROMS1, and ROMS2 simulations, respectively. The Gulf Stream velocity amplitudes become larger as the resolution of the simulations increase. This velocity increase can be explained by the flow becoming more inviscid at higher resolution and by the role of eddies in sharpening the mean current. It has been shown in the context of idealized quasigeostrophic (QG) models that the eddy-induced velocity accelerates the core of the western boundary current and decelerates its flanks ([Porta Mana and Zanna 2014](#)).

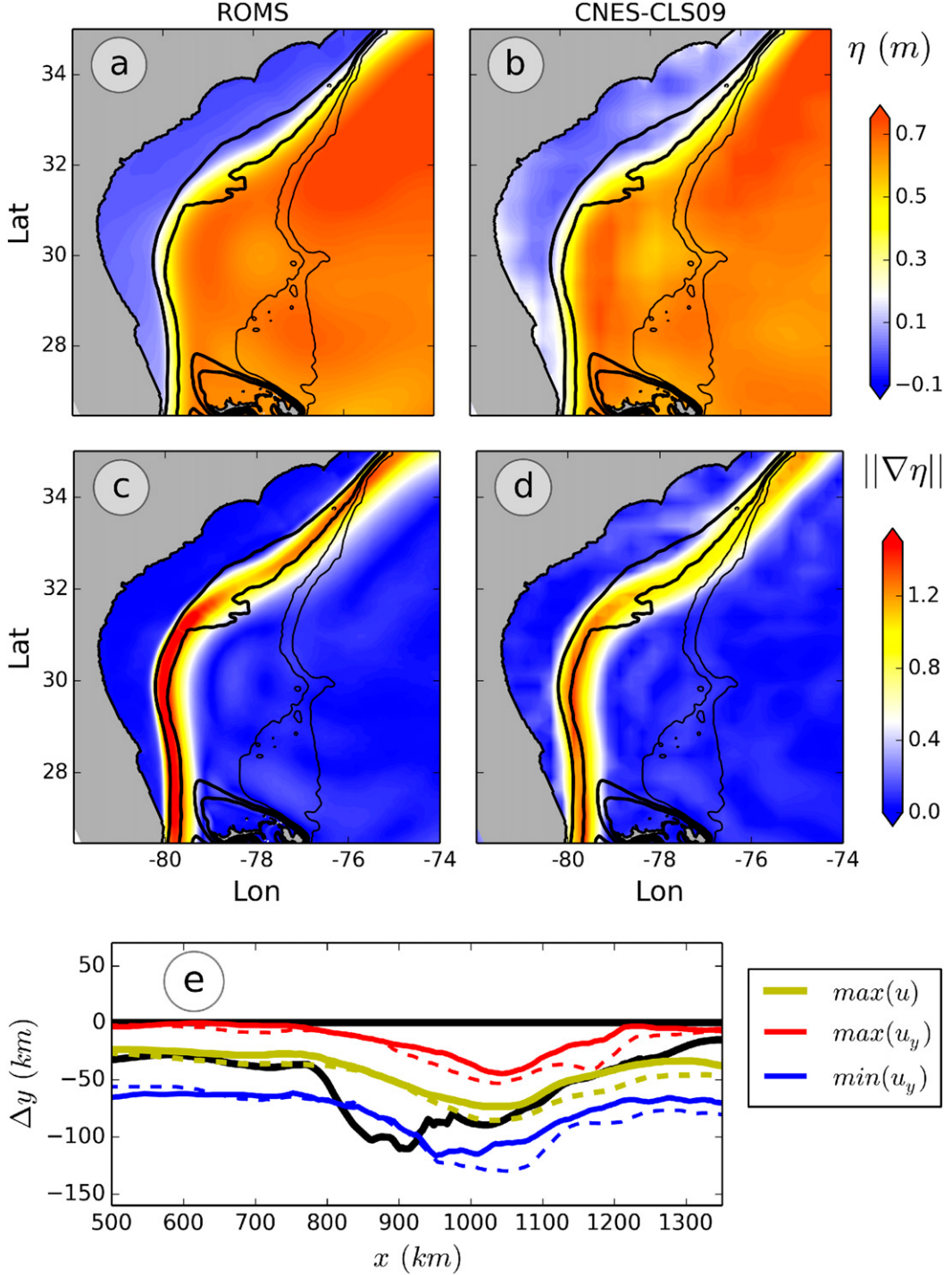


FIG. 4. (a) Mean sea surface height and (c) geostrophic currents from 18 yr of a  $\Delta x = 2.5$ -km horizontal resolution realistic ROMS simulation (ROMS1) and (b) observed mean dynamic topography and (d) geostrophic currents from the CNES-CLS09 dataset computed from the combination of GRACE data, altimetry, and in situ measurements (Rio et al. 2011). Sea surface heights in the top panels have been adjusted to have the same spatial mean over the domain. Topography is shown in black contours at 0-, 200-, 600-, 1000-, and 2000-m isobaths. (e) Location relative to the 200-m isobath of the maximum velocity (green) and the maximum (red) and minimum (blue) velocity shear for ROMS1 (solid lines) and for observations from the CNES-CLS09 dataset (dashed lines). Black lines show the location of the 200- and 600-m isobaths.

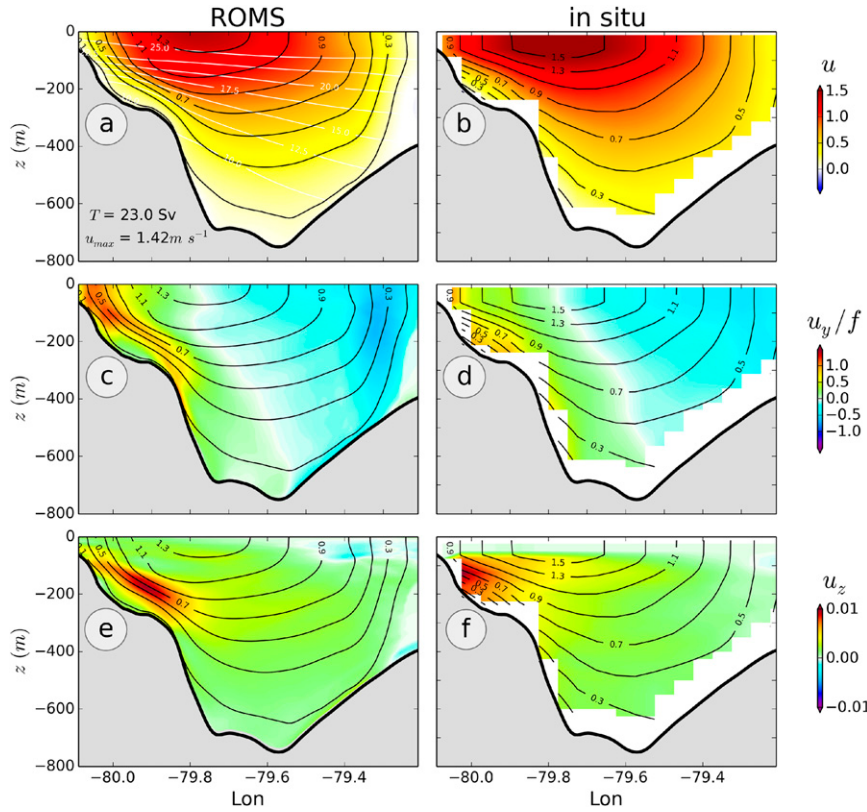


FIG. 5. (a),(b), Along-stream velocity  $u$  ( $\text{m s}^{-1}$ ), (c),(d) cross-stream velocity shear  $u_y/f$ , and (e),(f) vertical velocity shear  $u_z$  ( $\text{s}^{-1}$ ) in the Florida Strait at  $26^\circ\text{N}$  from (left) 1 yr of ROMS2 and (right) 5 yr of ADCP measurements from the Royal Caribbean Cruise Ship *Explorer of the Seas* (Beal et al. 2008). Black contours showing along-stream velocity  $u$  are repeated on all panels. White labeled contours in (a) show the temperature.

Vertical cross sections of velocity, cross-stream velocity shear  $u_y/f$ , and vertical velocity shear  $u_z$  are shown in Fig. 5 at  $26^\circ\text{N}$ , between Florida and the Bahamas, for 1 yr of ROMS2 and for 5 yr of ADCP measurements from a Caribbean cruise ship (Beal et al. 2008). The cross front and vertical structure of the velocities from the model are close to the observations. The cross-stream velocity shear is at its maximum close to the shelf break in the upper 200 m, and the vertical shear is at its maximum between 100- and 300-m depths above the slope. The amplitude of the velocities in the model is a little weaker at all depths, leading to a weaker 23-Sverdrups (Sv;  $1 \text{ Sv} \equiv 10^6 \text{ m}^3 \text{ s}^{-1}$ ) transport in ROMS2 compared to the 31-Sv transport estimated from measurements (Beal et al. 2008).

This weaker transport at the Florida Strait is mostly inherited from the parent simulations. The boundary of the ROMS1 and ROMS2 simulations are geographically close to the Florida Strait (Fig. 3), and the transport is constrained by the inflow from the parent Atlantic simulation ROMS0. Differences in transport and velocity amplitude among the different simulations become larger downstream as the

flow is reinforced by local recirculations whose intensity increases with the resolution of the model.

The transport of the Gulf Stream has been shown to increase substantially between the Straits of Florida and Cape Hatteras. According to Leaman et al. (1975), there is a transport increase right outside the Straits of Florida from 29 Sv at  $27^\circ\text{N}$  to 33 Sv at  $29^\circ\text{N}$  and a much larger threefold increase to about 93.7 Sv at  $73^\circ\text{W}$ , downstream from the Gulf Stream separation.

The barotropic streamfunction, showing the mean path of the Gulf Stream along the continental shelf and its transport, is shown in Fig. 6 for ROMS2. The U.S. coastline is defined as the 0-Sv contour. Vertical sections of velocity and temperature are plotted in Figs. 7 and 8 at different locations along the Gulf Stream path from upstream to downstream (Fig. 6), with values of the transport indicated on the corresponding panel. The different panels of Fig. 7 are located right after the Florida Strait (Fig. 7a), before (Fig. 7b), above (Fig. 7c) and downstream of the Charleston Bump, off Long Bay (Fig. 7d), between the bump and Hatteras off Onslow Bay (Fig. 7e), and where the stream rejoins the shelf edge

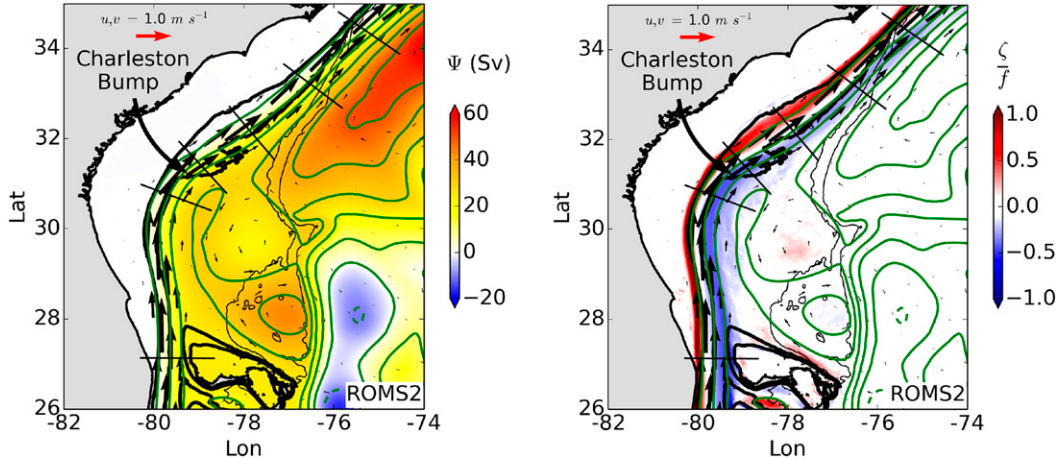


FIG. 6. (left) Mean barotropic streamfunction and (right) surface relative vorticity normalized by  $f$  for the Gulf Stream upstream of Cape Hatteras from 1 yr of ROMS2. Vectors are surface velocities. Barotropic streamfunction is shown in green with a 10-Sv interval. The U.S. coastline is defined as the 0-Sv contour, and the leftmost streamfunction contour corresponds to 1 Sv. Topography is shown in black contours at 0-, 200-, 600-, 1000-, and 2000-m isobaths. The straight black lines perpendicular to the streamflow show the locations of the vertical sections plotted in Figs. 7 and 8.

off Raleigh Bay (Fig. 7f). The transport increases from its initial 23 Sv at the 26°N section (Fig. 5) to 26 Sv at 27°N (Fig. 7a) and 32 Sv upstream of the Charleston Bump (Fig. 7b). It keeps increasing to 39 Sv downstream of the bump (Fig. 7d), 51 Sv off of Onslow Bay (Fig. 7e), and 57 Sv off of Raleigh Bay (Fig. 7f). After separation, the transport further increases very rapidly through confluence of the flow due to the Gulf Stream recirculation gyres. It reaches 85 Sv at 73°W in ROMS1 and peaks at 120 Sv in the region of the New England seamounts at 63°W (not shown).

The vertical and cross-section velocity structure of the flow is also varying along the way. The Gulf Stream is narrow, intense, and flowing against the slope in the Florida Strait (Fig. 7a). The flow increases its transport mostly by becoming wider after leaving the Florida Strait (Fig. 7b), while its vertical structure and velocity amplitude do not vary significantly. Maximum velocity values are 1.54 and 1.46  $\text{m s}^{-1}$  for the first two sections, respectively. Changes happen mostly when the flow reaches the Charleston Bump. The disruption and seaward deflection above the Charleston Bump are seen in Fig. 7c. The Gulf Stream loses contact with the slope on the side, but there is a strong interaction between the bottom of the flow and a part of the bump at  $z = -500$  m. The maximum velocity falls to 1.02 and 0.89  $\text{m s}^{-1}$  for sections plotted in Figs. 7c and 7d, respectively. The width of the flow does not change dramatically downstream of the bump, while the transport is doubled by Cape Hatteras. This strong increase in transport is associated mostly with the deepening of the flow and strengthening of the velocities. The

maximum velocities are slightly increased again to 1.09 and 1.11  $\text{m s}^{-1}$  for the sections shown in Figs. 7e and 7f, respectively.

The mean surface relative vorticity is also shown in Fig. 6. As expected, there is positive vorticity on the inshore side of the Gulf Stream and negative vorticity on the seaward side according to the sign of the shear of the mean flow. The amplitude of the positive vorticity is larger than the amplitude of the negative vorticity, that is, the inshore side of the Gulf Stream is sharper. Negative values of the vorticity are strongly limited by the condition on centrifugal instability ( $\zeta < -f$ ), while there is no such limit on the positive  $\zeta$  values (Thomas et al. 2013).

Vertical sections of relative vorticity are plotted in Fig. 7 along the Gulf Stream path. In the first two panels (Figs. 7a,b), upstream of the Charleston Bump, the flow is strongly squeezed against the slope on the inshore side, which makes the velocity shear and positive vorticity large in both sections. Maximum and minimum relative vorticity values are  $4.44f$  and  $-8.95f$  for the first section and  $2.46f$  and  $-0.44f$  for the second one, as specified in the caption of Fig. 7. The stream is flowing along topography on both sides in the first section such that negative values are also generated in localized regions on the eastern side of the flow at about 150–200-m depth along the slope of the Little Bahama Bank. This forms a quasi-permanent narrow strip of highly negative vorticity that is dissipated shortly through intense small-scale inertial (or centrifugal) instability. The disruption and broadening of the flow at the Charleston Bump in Figs. 7c and 7d lead to a decrease of the maximum vorticity values to  $0.90f$  and  $0.82f$ , respectively. Downstream

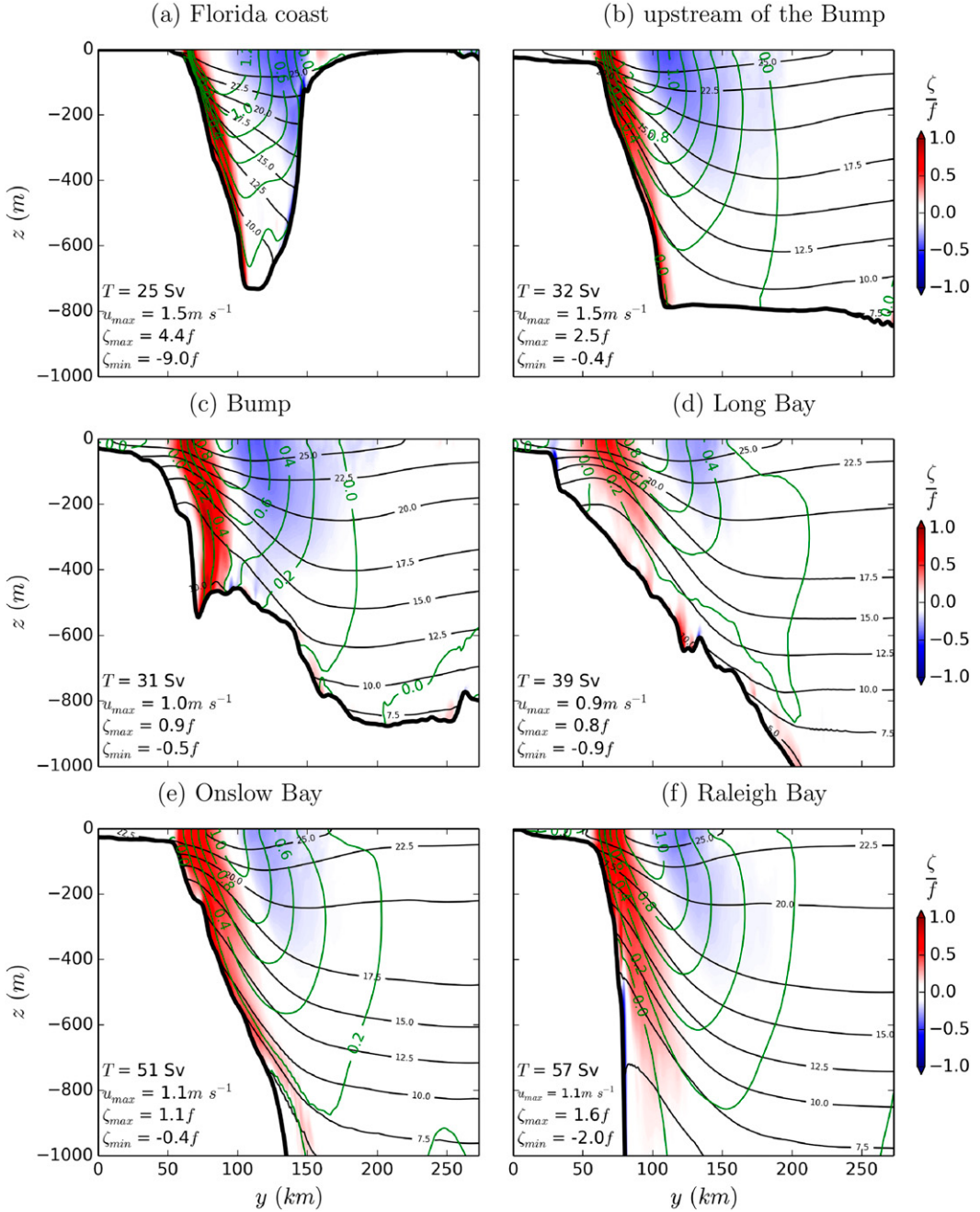


FIG. 7. Mean relative vorticity normalized by  $f$  (colors), temperature (black contours), and along-stream velocity (green contours) for ROMS2 along the vertical cross-shelf sections marked as black dashed lines in Fig. 6. Panels are plotted from upstream to downstream. The local along-stream and cross-stream directions are defined relative to the  $\Psi = 1$  streamline plotted as the inshore green line in Fig. 6. Maximum and minimum relative vorticity values for each section are (a) 4.44 and  $-8.95$ , (b) 2.46 and  $-0.44$ , (c) 0.90 and  $-0.48$ , (d) 0.82 and  $-0.85$ , (e) 1.06 and  $-0.43$ , and (f) 1.62 and  $-1.96$ .

of the bump, the stream is squeezed against the slope, and maximum vorticity values increase again to reach  $1.06f$  and  $1.62f$  in Figs. 7e and 7f, respectively. Minimum vorticity values in the anticyclonic side of the stream do not vary significantly downstream of section Fig. 7b. The

minimum value of  $-0.90f$  indicated in Fig. 7d is located at  $z = -100$  m on the shoreward side and is a result from the weak mean southwestward current created by the quasi-permanent Charleston Gyre flowing along the slope. There is again a narrow strip of highly negative vorticity

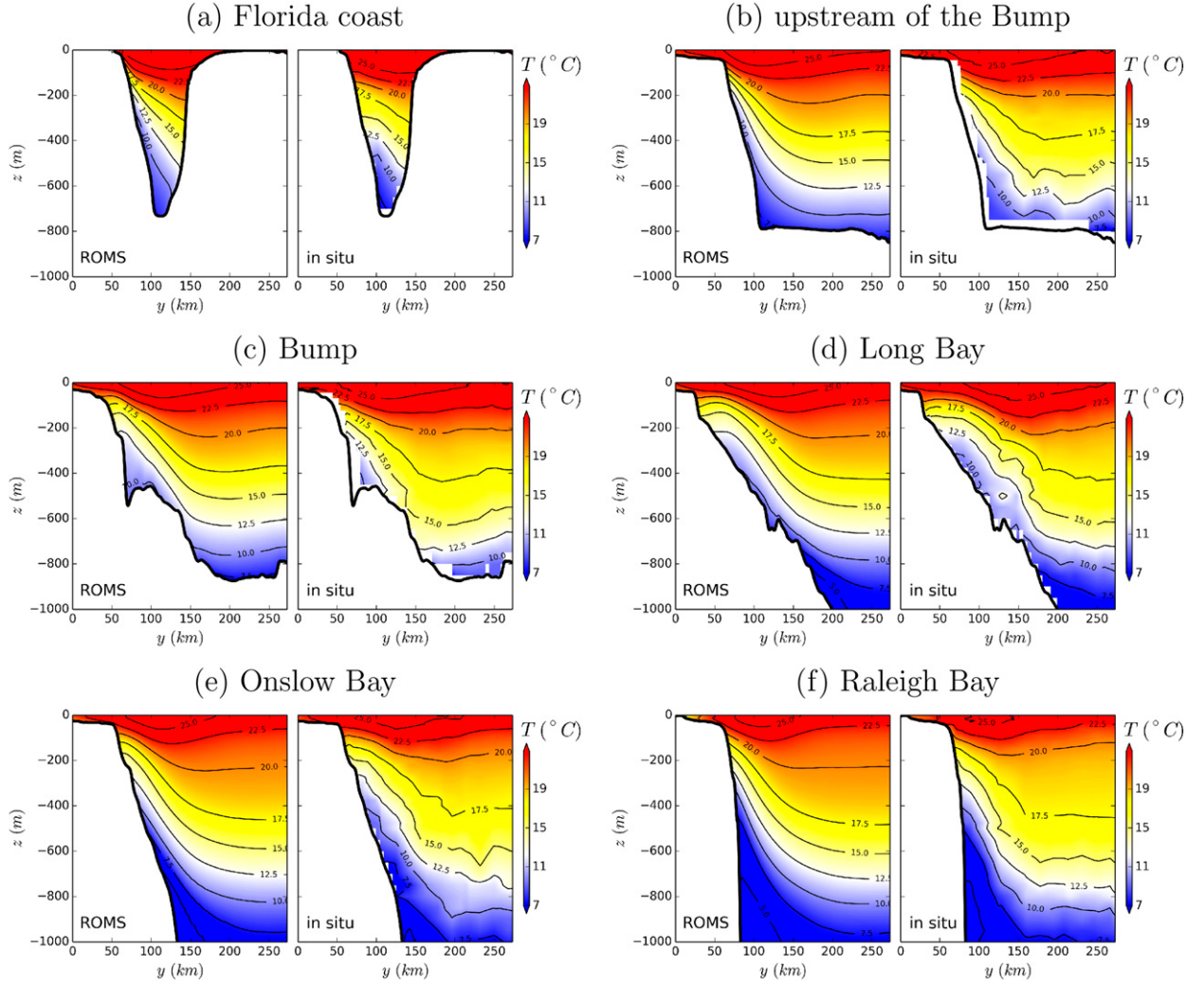


FIG. 8. Annual-mean temperature for ROMS2 and statistical-mean temperature from in situ profile data (WOA; Locarnini et al. 2013) along the vertical cross-shelf sections marked as black dashed lines in Fig. 6. Panels are plotted from upstream to downstream. The local along-stream and cross-stream directions are defined relative to the  $\Psi = 1$  streamline plotted as the inshore green line in Fig. 6.

(down to  $-1.96f$ ) along the shelf below  $z = -500$  m in Fig. 7f. This corresponds to negative vorticity generation by the deep western boundary current that is flowing locally southwestward and crosses below the Gulf Stream at Cape Hatteras.

Cross sections of temperature have been compared to different datasets such as objectively analyzed mean fields from the WOA (Locarnini et al. 2013) and the SODA ocean climatology outputs (Carton and Giese 2008). They show a very good correspondence for the vertical structure at  $\approx 150$  km from the coast, but both datasets are unable to accurately resolve the tilting of the isotherms close to the coast. To resolve the structure of the isotherms close to the coast, we use statistical means of the in situ profile data used to construct the WOA climatology binned to a  $1/4^\circ \times 1/4^\circ$  Cartesian grid.

The vertical structure of the model temperature is in very good agreement with the in situ data at each section (Fig. 8). The spreading of the  $17.5^\circ$  and  $20^\circ\text{C}$  isotherms in the anticyclonic flank of the Gulf Stream seen in the model downstream of the bump (Figs. 8d,e,f) is also visible in observations. It is a signature of the presence of the North Atlantic Subtropical Mode Water, also known as Eighteen Degree Water, which sits northeast of the bump.

#### b. Variability of the Gulf Stream at the bump

Observations show a sharp increase in the variance of the stream position at the bump (Olson et al. 1983). The Gulf Stream position downstream of the Charleston Bump is described by Bane and Dewar (1988) as having a bimodal character with a weakly deflected state, where the shoreward Gulf Stream front remains inshore of the

600-m isobath, and a strongly deflected state where the front is located offshore of the 600-m isobath. Snapshots of SST are shown in Fig. 9 along the sketches of Bane and Dewar (1988) to illustrate the presence of the two Gulf Stream states in the model.

To investigate the temporal variability of the Gulf Stream at the bump, we compute the free-surface height time series and probability density functions at different locations along the Gulf Stream path, following an isoline of mean free-surface height (Fig. 10). There is a clear increase in variability over the bump at 32°N, as shown by the spreading of the density function in Fig. 10d compared to Figs. 10a–c. The shape of the density function also changes dramatically as two smaller peaks form instead of a large central one, demonstrating the bimodal character of the stream over the bump. The density function still exhibits two peaks at 33°N (Fig. 10e) but not at 34°N (Fig. 10f).

Satellite altimetry, with data available for the last 20 yr, provides the best estimate of the scales and patterns of the surface mesoscale variability. We compare in Fig. 11 the mean free-surface variability  $\overline{\eta^2}$  from the model with altimetric observations. The patterns of free-surface variability are similar to the patterns of surface eddy kinetic energy (EKE) as described by Ducet and Le Traon (2001). Altimetric observations are the 1992–2012 AVISO sea level anomalies ([www.aviso.altimetry.fr](http://www.aviso.altimetry.fr)), which are originally mapped on a  $1/4^\circ \times 1/4^\circ$  Cartesian grid. The smaller scales are filtered from the model by smoothing fields at each time step using a convolution with a 30-km half-width Gaussian kernel to match approximately the resolution of the observations.

The model and altimetric data display similar scales and patterns of enhanced variability. The mesoscale variance is identically strong in both models and observations in a rather narrow band along the Gulf Stream path north of 31.5°N over and to the northeast of the bump, with a maximum at 32°N at the location of Fig. 10d. Other regions of strong variance in the Sargasso Sea, south and east of the bump, are also well reproduced in the model.

#### 4. Topographic influence on the Gulf Stream

It is evident from the description of its path, vertical structure, and variability that the dynamics of the Gulf Stream along the seaboard is at least partly controlled by the topography. The Charleston Bump, in particular, exerts a strong influence on the flow as seen from the quasi-permanent deflection of the stream.

##### a. Bottom pressure forces and torque around the bump

The impact of the Charleston Bump on the flow can be discussed in terms of bottom pressure and form drag.

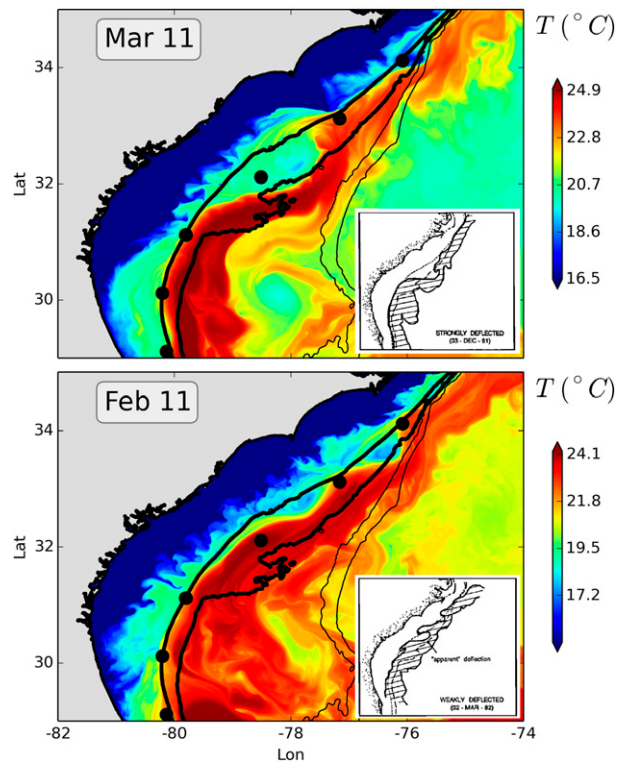


FIG. 9. Instantaneous SST for the Gulf Stream as simulated by ROMS2 showing a (top) typical strongly deflected configuration and a (bottom) weakly deflected configuration as defined in Bane and Dewar (1988). Insets show corresponding sketches, retracted from AVHRR SST images, taken from Bane and Dewar (1988). Topography is shown in black contours by the 0-, 200-, 600-, 1000-, and 2000-m isobaths.

The form drag is the force that results from pressure differences across an obstacle in the flow. It should not be confused with the bottom drag that represents the turbulent boundary layer processes at the bottom. The bottom pressure  $p_b = p[x, y, z_b(x, y), t]$  can be partitioned into a large static pressure environment  $O(10^7) \text{ N m}^{-2}$  and a small dynamic part  $O(100) \text{ N m}^{-2}$ . The local interpretation of the dynamic bottom pressure represents a dominant balance with inertial forces. As currents flow around bottom features, inertia has to be balanced by pressure forces against the bottom. Form drag is not a direct energy sink, contrary to the viscous bottom drag, but it does allow an energy conversion from the along-flow-averaged flow to steady standing eddies in addition to indirect effects of altering the conversion from the mean state to transient eddies.

To accurately evaluate the bottom pressure and the form drag we use the diagnostic procedure detailed in Molemaker et al. (2015). We make use of the relation between bottom pressure anomalies and bottom pressure

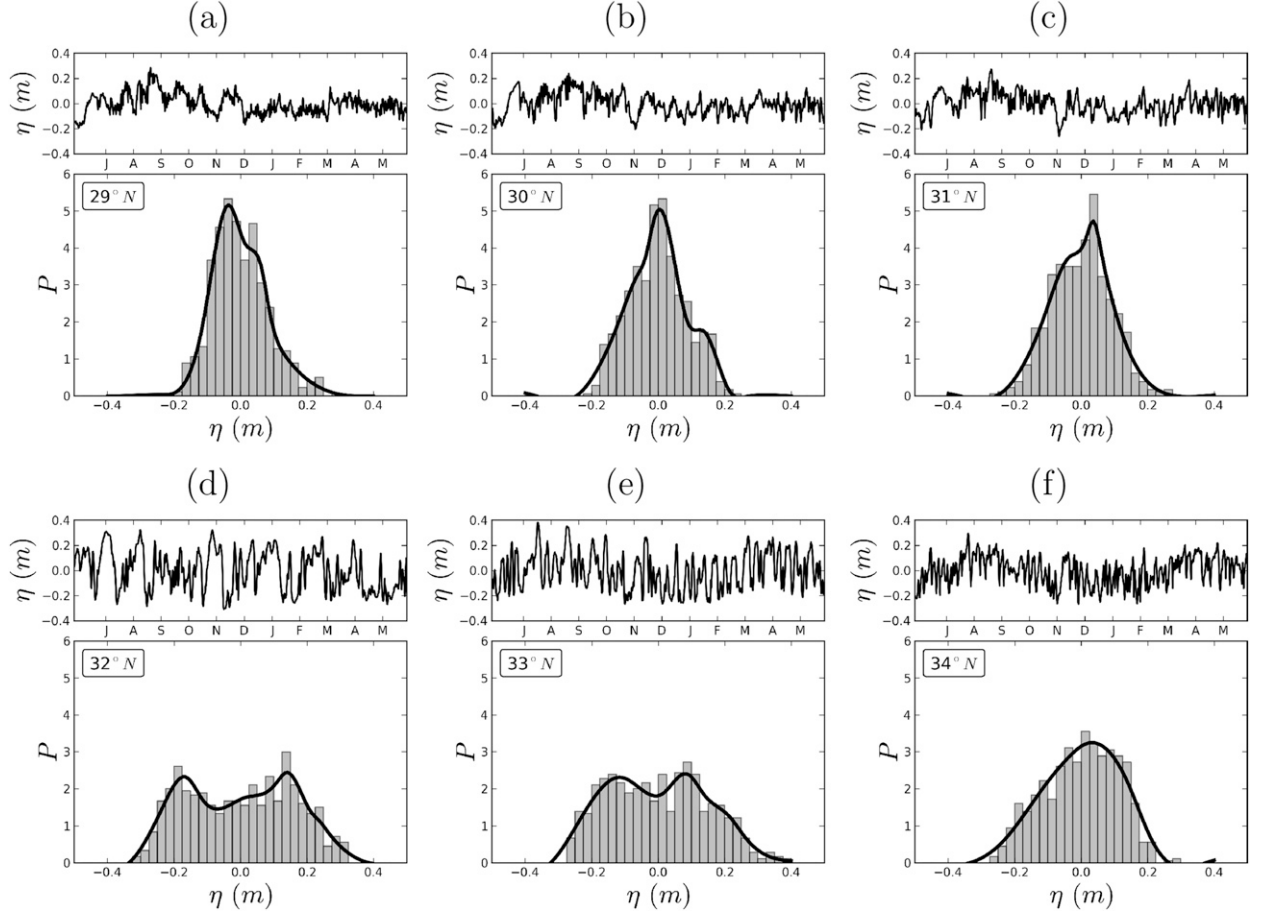


FIG. 10. Pointwise time series and probability density functions of free-surface height  $\eta$  at different locations, from upstream to downstream, along the Gulf Stream path for 1 yr of ROMS2. These locations are shown as black dots in Fig. 9 and are located on one isoline of free-surface height at latitudes (a)  $29^{\circ}\text{N}$ , (b)  $30^{\circ}\text{N}$ , (c)  $31^{\circ}\text{N}$ , (d)  $32^{\circ}\text{N}$ , (e)  $33^{\circ}\text{N}$ , and (f)  $34^{\circ}\text{N}$ .

torque  $\mathbf{J}(P_b, h)$ , which is the Jacobian of the bottom pressure and the depth of the topography  $h$ . For a terrain-following model like ROMS, the bottom torque can be computed exactly by taking the curl of the vertically integrated horizontal pressure gradient (Song and Wright

1998). From the torque we can find a pressure anomaly along a contour line of fixed topography depth using

$$p_b = - \int \frac{\partial \mathbf{J}(P_b, h)}{\partial h/\partial n} ds. \quad (1)$$

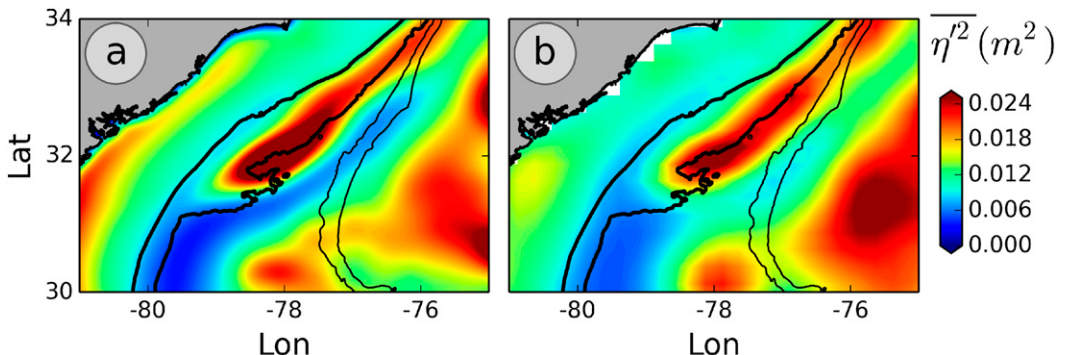


FIG. 11. Free-surface variability  $\overline{\eta^2}$  ( $\text{m}^2$ ) for (a) ROMS2 smoothed using a 30-km half-width Gaussian and (b) observations from AVISO. Topography is shown in black contours by the 0-, 200-, 600-, 1000-, and 2000-m isobaths.

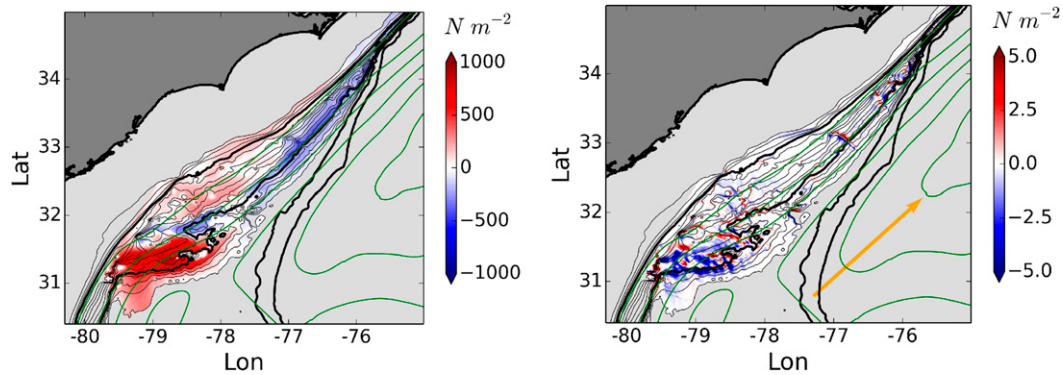


FIG. 12. (left) Mean bottom pressure anomaly and (right) form drag contribution along the direction of the flow over the Charleston Bump area for ROMS2. Topography is shown in thick black contours at 0-, 200-, 600-, 1000-, and 2000-m isobaths and in thin black contours every 50 m between 50 and 800 m. Barotropic streamfunction is shown in green with a 10-Sv interval.

The variables  $(n, s)$  are right-handed horizontal coordinates with  $s$  as the distance along a contour. The quantity  $\partial h/\partial n$  is the local slope, oriented to the right of the direction of integration. Using this approach we can accurately compute the local bottom pressure anomaly up to an integration constant.

The bottom pressure anomaly at the location of the Charleston Bump is shown in Fig. 12. The integration domain starts right upstream of the bump, where the bottom pressure anomaly along each topography contour is initialized at zero and extends to Cape Hatteras, between the 100- and 800-m isobaths. There is, as expected, high positive bottom pressure on the upstream side of the bump and negative bottom pressure on the downstream side. The negative bottom pressure has a smaller amplitude but extends over a larger area in the downstream direction. The positive pressure anomaly forces the current above and around the bump, changing its mean direction to locally eastward. The negative pressure anomaly on the downstream side of the bump allows the current to progressively change back its direction to northward.

The corresponding form drag shown Fig. 12b is computed by multiplying the pressure anomalies with the bottom slope in the mean direction of the flow (indicated by an arrow in Fig. 12b). The form drag pattern implies a net force in the upstream direction, so the form drag is retarding the Gulf Stream in this location. The integral force for the permissible area around the bump (corresponding to the unshaded area in Fig. 12) is  $1.5 \times 10^{10}$  N. An integral of the turbulent bottom drag contribution over the same area leads to a value of  $0.3 \times 10^{10}$  N, about 5 times smaller than the form drag contribution. The area of the surface is  $5 \times 10^{10}$  m<sup>2</sup>. This implies a mean force of  $0.3 \text{ N m}^{-2}$  due to the form drag over the area. This can be compared to more familiar surface wind

stress values  $\leq 0.05 \text{ N m}^{-2}$  in the region, which is similar to the average turbulent bottom drag value here.

The bottom pressure torque  $\mathbf{J}(P_b, h)$  arises from the variation of bottom pressure along isobaths. It derives from the twisting of the force that the bottom topography exerts on the ocean. The mean bottom pressure torque is shown in Fig. 13a. The signal strongly reflects the regional topography with large positive-negative signals around small-scale topography features. To see the larger-scale contribution of the bottom pressure torque, we smooth horizontally the mean bottom pressure torque by using a convolution with a Gaussian kernel of half-width 10 km in Fig. 13b. The large negative signal where the stream encounters the tip of the bump ( $31^\circ\text{N}, 79.5^\circ\text{W}$ ) corresponds to the incoming flow going uphill. There are two large positive signals downstream on both sides of the stream where the flow is locally going downhill, followed by smaller negative signals where the flow is going uphill again.

The bottom pressure torque is closely related to the bottom vortex stretching term (e.g., Zhang and Vallis 2007). It is possible to write the relation  $-\mathbf{f}\mathbf{u}_b \cdot \nabla h = [\mathbf{J}(P_b, h)]/\rho_0$  for an idealized linear case of a current in geostrophic balance with a free-slip condition at the bottom. Given the kinematic condition at the bottom  $\omega_b = -\mathbf{u}_b \cdot \nabla h$ , the bottom pressure torque could then be written  $[\mathbf{J}(P_b, h)]/\rho_0 = -f\omega_b$ , which is the bottom vortex stretching. This is not true in general because of the ageostrophic and viscous effects at the bottom, but the bottom vortex stretching is locally the leading order in the bottom pressure torque signal around the bump.

#### b. Barotropic vorticity balance

The bottom pressure torque represents the contribution of the topography to the barotropic vorticity evolution of

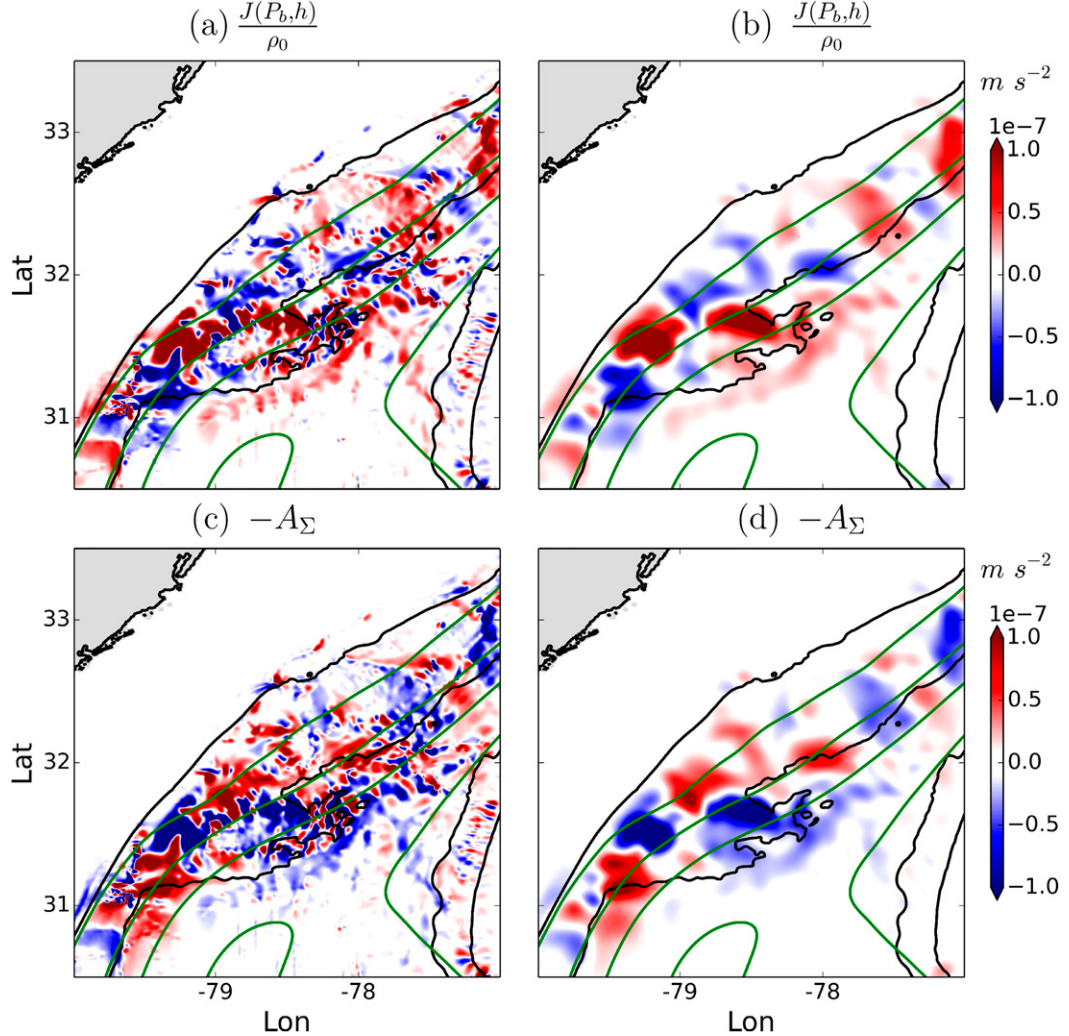


FIG. 13. Time mean ( $\text{m s}^{-2}$ ) of (a),(b) bottom pressure torque  $\mathbf{J}(P_b, h)/\rho_0$ , and (c),(d) nonlinear advective terms in the barotropic vorticity balance equation  $-A_\Sigma$  for ROMS2. (b) and (d) are horizontally smoothed by using a convolution with a Gaussian kernel of half-width 10 km. Topography is shown in black contours at 0-, 200-, 600-, 1000-, and 2000-m isobaths. Barotropic streamfunction is shown in green with a 10-Sv interval.

the flow. Hughes (2000), Hughes and De Cuevas (2001), and Jackson et al. (2006) show by using theoretical arguments, numerical results for an idealized gyre simulation, and realistic simulations from a large-scale global model that western boundary currents do not imply a viscous balance against the seaboard (as in the traditional view based on models with flat bottoms and vertical sidewalls) but a nearly inviscid one. The bottom

pressure torque is the term locally enabling the return flow of the wind-driven transport in western boundary currents and providing most of the overall positive input of vorticity balancing the negative input by anticyclonic wind curl on the scale of the gyre.

The full barotropic vorticity balance equation of the flow is obtained by integrating the momentum equations in the vertical and cross-differentiating them:

$$\underbrace{\frac{\partial \Omega}{\partial t}}_{\text{rate}} = - \underbrace{\nabla \cdot (f \bar{\mathbf{u}})}_{\text{planet.vort.adv.}} + \underbrace{\frac{\mathbf{J}(P_b, h)}{\rho_0}}_{\text{bot.pres.torque}} + \underbrace{\mathbf{k} \cdot \nabla \times \frac{\boldsymbol{\tau}^{\text{wind}}}{\rho_0}}_{\text{wind curl}} - \underbrace{\mathbf{k} \cdot \nabla \times \frac{\boldsymbol{\tau}^{\text{bot}}}{\rho_0}}_{\text{bot.drag curl}} + \underbrace{\mathcal{D}_\Sigma}_{\text{horiz.diffusion.}} - \underbrace{A_\Sigma}_{\text{NL advection}}, \quad (2)$$

where the barotropic vorticity is defined as the vorticity of the vertically integrated velocities

$$\Omega = \frac{\partial \bar{v}}{\partial x} - \frac{\partial \bar{u}}{\partial y},$$

with  $(u, v)$  as the  $(x, y)$  components of the horizontal flow, and the overbar denotes a vertically integrated quantity

$$\bar{u} = \int_{-h}^{\zeta} u dz,$$

where  $\eta(x, y, t)$  is the free-surface height, and  $h(x, y) > 0$  is the depth of the resting topography. The equation  $H(i, j, t) = \int_{-h}^{\eta} dz = \eta(i, j, t) + h(i, j)$  defines the total depth of the water column. Note that the barotropic vorticity is not identical to the vertically integrated vorticity. The curl and the vertical integration can be interchanged at the expense of introducing terms because of the horizontal variations of the limits of the integral. The difference  $\Omega - \bar{\zeta} = \mathbf{u}_s \times \nabla \eta + \mathbf{u}_b \times \nabla h$ , where  $\mathbf{u}_s$  and  $\mathbf{u}_b$  are the horizontal velocities at the surface and bottom, respectively, can be nonnegligible at places where we have both significant bottom currents and large topography slopes. Finally, the curl of nonlinear advection terms can be written as

$$A_{\Sigma} = \frac{\partial^2(\bar{v}\bar{v} - \bar{u}\bar{u})}{\partial x \partial y} + \frac{\partial^2 \bar{v}\bar{v}}{\partial x \partial x} - \frac{\partial^2 \bar{u}\bar{u}}{\partial y \partial y},$$

and  $D_{\Sigma}$  is the term due to the horizontal diffusion in the model implicitly part of the advection in ROMS.

The nonlinear advective term  $-A_{\Sigma}$  is also plotted in Figs. 13c and 13d along the bottom pressure torque, with and without horizontal smoothing. There is locally a very large cancellation between  $-A_{\Sigma}$  and  $\mathbf{J}(P_b, h)/\rho_0$ . This results from the balance between pressure forces and inertia around small-scale topographic features. We plot the sum of the two terms  $[\mathbf{J}(P_b, h)/\rho_0] - A_{\Sigma}$  along the entire seaboard in Fig. 14a. Note that the scale has been divided by 5 in Fig. 14 compared to Fig. 13. Most of the intense small-scale structures are gone. The other significant terms in the barotropic vorticity balance equation—the bottom drag curl  $-\mathbf{k} \cdot \nabla \times (\tau^{\text{bot}}/\rho_0)$  and the planetary vorticity advection  $-\nabla \cdot (f \bar{\mathbf{u}})$ —are plotted in Figs. 14b and 14d, respectively. We do not plot the rate of change of vorticity  $\partial \Omega / \partial t$ , the horizontal diffusion  $D_{\Sigma}$ , and the wind stress curl  $-\mathbf{k} \cdot \nabla \times (\tau^{\text{wind}}/\rho_0)$  because they are all at least an order of magnitude smaller compared to the others.

Both the terms  $[\mathbf{J}(P_b, h)/\rho_0] - A_{\Sigma}$  and the bottom drag curl in Figs. 14a and 14b still exhibit some very small-scale signals related to topography details. These details disappear in the sum  $[\mathbf{J}(P_b, h)/\rho_0] - A_{\Sigma} - \mathbf{k} \cdot \nabla \times (\tau^{\text{bot}}/\rho_0)$ , plotted

in Fig. 14c without any spatial smoothing. This term balances well the meridional transport of planetary vorticity plotted in Fig. 14d. The remaining small differences between Figs. 14c and 14d are due to the residual  $\partial \Omega / \partial t$  and would require additional years of simulation to be completely smoothed out.

Spatial integrals of all the barotropic vorticity balance terms over the area plotted in Fig. 14 confirm that bottom pressure torque and meridional transport are the only contributing terms (Fig. 15). Bottom pressure torque is crucial in steering the Gulf Stream and returning it in the gyre. The nonlinear term accounts mostly for permanent meanders and transient eddies that act to redistribute locally vorticity inside the stream, but do not contribute significantly in an integral sense. The bottom drag curl is responsible for local modifications at the Charleston Bump by weakening vorticity amplitude on both sides of the stream but does not contribute either in an integral sense over this area. The wind stress curl input is small because the area of integration is small, but it will become a dominant term in the balance once integrated over the whole gyre.

The inviscid character of the Gulf Stream along the seaboard, in the form of a first-order balance between meridional transport and bottom pressure torque, is demonstrated here in the context of a fully realistic setup with eddy-resolving resolution. We compute different terms of the barotropic vorticity equation with unprecedented accuracy, aided by the properties of the terrain-following vertical coordinate formulation of the model that is discretely conservative for barotropic vorticity, and find a high degree of balance between inertial forces, bottom pressure torque, and the advection of planetary vorticity. Horizontal diffusion has a much smaller magnitude and bottom drag is only significant in a few, localized places (Fig. 14b).

In addition to this finding, we show that at small scales there is a first-order balance between inertia and bottom pressure torque. As the flow follows contours of topography, bottom pressure torque overcomes inertia and forces the flow on curved trajectories. This is an important insight that allows one to view the process of flow separation from the topography in terms of the *absence* of a pressure torque, rather than the *presence* of a separating force. Underneath this small-scale first-order balance between inertia and pressure torque is the balance with planetary vorticity advection as visible in Fig. 14.

## 5. Eddy-mean interaction

The topography not only impacts the mean Gulf Stream directly through bottom pressure and form drag by steering and retarding the flow, but also indirectly by modifying the stability properties of the flow that modulate the

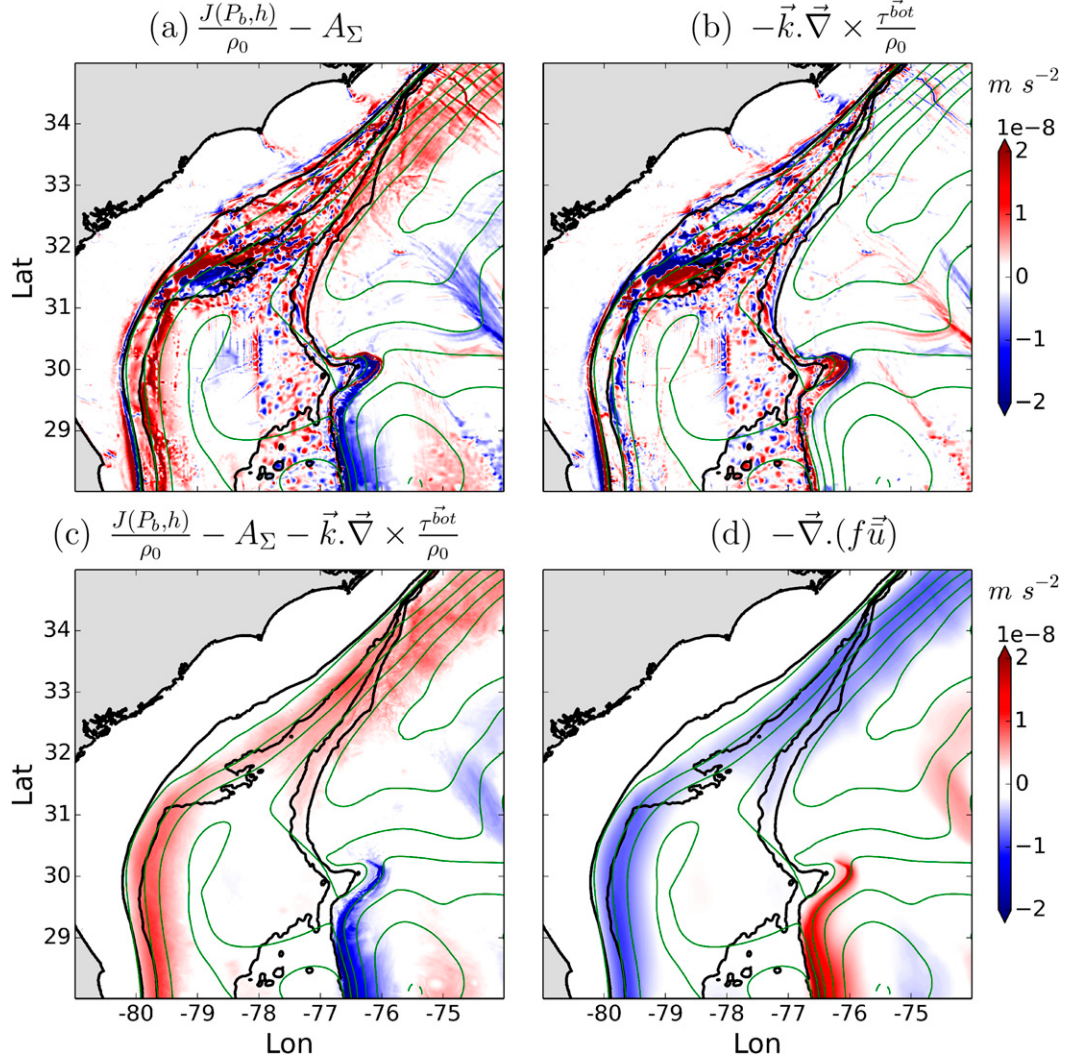


FIG. 14. Time mean ( $\text{m s}^{-2}$ ) of the different terms in the barotropic vorticity balance equation: (a)  $[\mathbf{J}(P_b, h)/\rho_0] - A_\Sigma$ , (b) bottom drag curl  $-\mathbf{k} \cdot \nabla \times (\tau^{\text{bot}}/\rho_0)$ , (c) sum of (a) and (b)  $[\mathbf{J}(P_b, h)/\rho_0] - A_\Sigma - \mathbf{k} \cdot \nabla \times (\tau^{\text{bot}}/\rho_0)$ , and (d) planetary vorticity term  $-\nabla \cdot (f \bar{\mathbf{u}})$  for ROMS2. Topography is shown in black contours at 0-, 200-, 600-, 1000-, and 2000-m isobaths and mean barotropic streamfunction in green lines (contours every 10 Sv).

mean–eddy interactions. The eddies provide an important mechanism to maintain and shape the mean current as their nonlinear interactions impact its strength, structure, and stability. The questions addressed in this section are (i) where are the eddies generated? (ii) What are the mechanisms responsible for their generation? (iii) What is the impact of the topography on these mechanisms? (iv) How are the properties of the mean flow modified through nonlinear eddy–mean flow interactions?

#### a. Energy conversion

To investigate the nature of the instability processes that generate the eddies, it is useful to look at the source of eddy energy. We can write all variables as  $u = \langle u \rangle + u'$ , where the brackets denote a time average and the prime

denotes the fluctuation part. The mean kinetic to eddy kinetic energy conversion, which can be divided into contributions from the horizontal Reynolds stress (HRS) and the vertical Reynolds stress (VRS), is written as

$$K_m K_e = \text{HRS} + \text{VRS}, \quad (3)$$

where

$$\text{HRS} = -\langle u'^2 \rangle \frac{\partial \langle u \rangle}{\partial x} - \langle u' v' \rangle \frac{\partial \langle u \rangle}{\partial y} - \langle v'^2 \rangle \frac{\partial \langle v \rangle}{\partial y} - \langle u' v' \rangle \frac{\partial \langle v \rangle}{\partial x} \quad (4)$$

corresponds to the product of horizontal mean shear and horizontal Reynolds stress, and

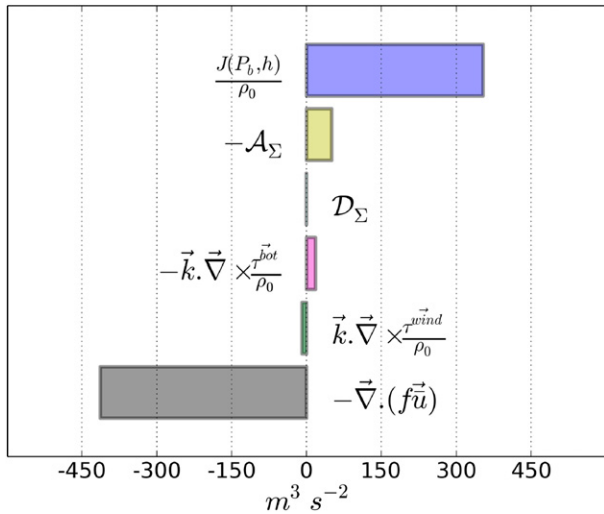


FIG. 15. Spatial integral of the vorticity balance equation terms ( $\text{m}^3 \text{s}^{-2}$ ) over the domain plotted in Fig. 14: bottom pressure torque  $\mathbf{J}(P_b, h)/\rho_0$ , nonlinear advective terms  $-A_\Sigma$ , horizontal diffusion  $D_\Sigma$ , bottom drag curl  $-\mathbf{k} \cdot \nabla \times (\tau^{01}/\rho_0)$ , wind stress curl  $-\mathbf{k} \cdot \nabla \times (\tau^{wind}/\rho_0)$ , and planetary vorticity term  $-\nabla \cdot (f \bar{\mathbf{u}})$  for ROMS2.

$$\text{VRS} = -\langle u'w' \rangle \frac{\partial \langle u \rangle}{\partial z} - \langle v'w' \rangle \frac{\partial \langle v \rangle}{\partial z} \quad (5)$$

arises from vertical shear of the mean flow and vertical Reynolds stress. The eddy potential to eddy kinetic energy conversion is the vertical eddy buoyancy flux

$$P_e K_e = \langle w'b' \rangle, \quad (6)$$

where  $b$  is the buoyancy anomaly relative to the local area average. The mean potential to mean kinetic energy conversion is

$$P_m K_m = \langle w \rangle \langle b \rangle. \quad (7)$$

The mean potential to mean eddy energy conversion  $P_m K_m$  (Fig. 16a) points out the standing eddy signal. Large amplitudes correspond to the stream flowing over the bump and the deep western boundary current flowing around the Blake Nose and following the Blake Escarpment southward. No work can be done by the bottom pressure force, and it does not provide any energy tendency, but it can induce an energy conversion between the time- and along-flow mean current and the time-mean standing eddies (Molemaker et al. 2015). According to the bottom pressure anomaly pattern plotted in Fig. 12a, the conversion is positive at the tip of the bump, where potential is converted to mean kinetic energy, and negative over the bump, where kinetic energy is converted back to mean potential energy. This

implies energy conversion from the mean flow to the mean standing eddies.

Mechanisms responsible for the generation of transient eddies can be identified by looking at the source terms for the EKE:  $\langle w'b' \rangle$ , HRS, and VRS. Predominance of one of the three source terms indicates that the eddy generation mechanism is primarily a baroclinic instability ( $\langle w'b' \rangle > 0$ ), a barotropic instability (HRS  $> 0$ ), or a vertical shear (Kelvin–Helmholtz type) instability (VRS  $> 0$ ). The baroclinic ( $\langle w'b' \rangle$ ; Fig. 16b) and barotropic (HRS; Fig. 16c) conversion terms both have strong positive signals at the bump and at Cape Lookout, showing that these are regions of eddy generation from mixed baroclinic–barotropic origin. The patterns of both signals at the Charleston Bump exhibit some variations. The baroclinic conversion has a subsurface maximum centered on  $z = -400 \text{ m}$  and is more intense seaward, while the barotropic conversion is surface intensified and is more intense on the inshore side of the flow, in agreement with the subsurface observations of Dewar and Bane (1985). The part of the eddy kinetic energy conversion due to the VRS (Fig. 16d) is much smaller everywhere. It is, however, interesting to note the negative signal at Cape Lookout is barely visible in the lower-resolution simulation ROMS0 (not shown) but becomes significant in the higher-resolution simulation ROMS2.

In addition to the strong signals at the bump and Cape Lookout, there is a smaller negative baroclinic conversion downstream of the bump on the inshore side. The weak, positive baroclinic conversions seen along the Sargasso Sea side of the stream, mostly confined in the surface layer, is related to mixed layer baroclinic instability (MLI; Boccaletti et al. 2007).

The barotropic conversion has a very distinctive pattern of alternating positive and negative signals (Fig. 16c). The conversion is weakly negative south of  $27^\circ\text{N}$ , positive between  $27^\circ$  and  $30^\circ\text{N}$ , negative upstream of the bump between  $30^\circ$  and  $31^\circ\text{N}$ , positive over the bump, negative again downstream of the bump, and finally positive off of Cape Lookout. These regions of negative HRS are also regions with negative or very weak baroclinic conversion such that the net energy conversion is from eddy to mean. These patterns correspond to the energy budgets of the eddy and mean flow upstream and downstream of the Charleston Bump measured by Hood and Bane (1983) and Dewar and Bane (1985). They both measured a large conversion of mean-to-eddy energy at the bump and eddy-to-mean energy downstream of the bump. Webster (1961) also showed that the eddy-to-mean conversion downstream of the bump was happening especially in a 20-km-wide zone in the region of cyclonic shear, which is also seen in Fig. 16c.

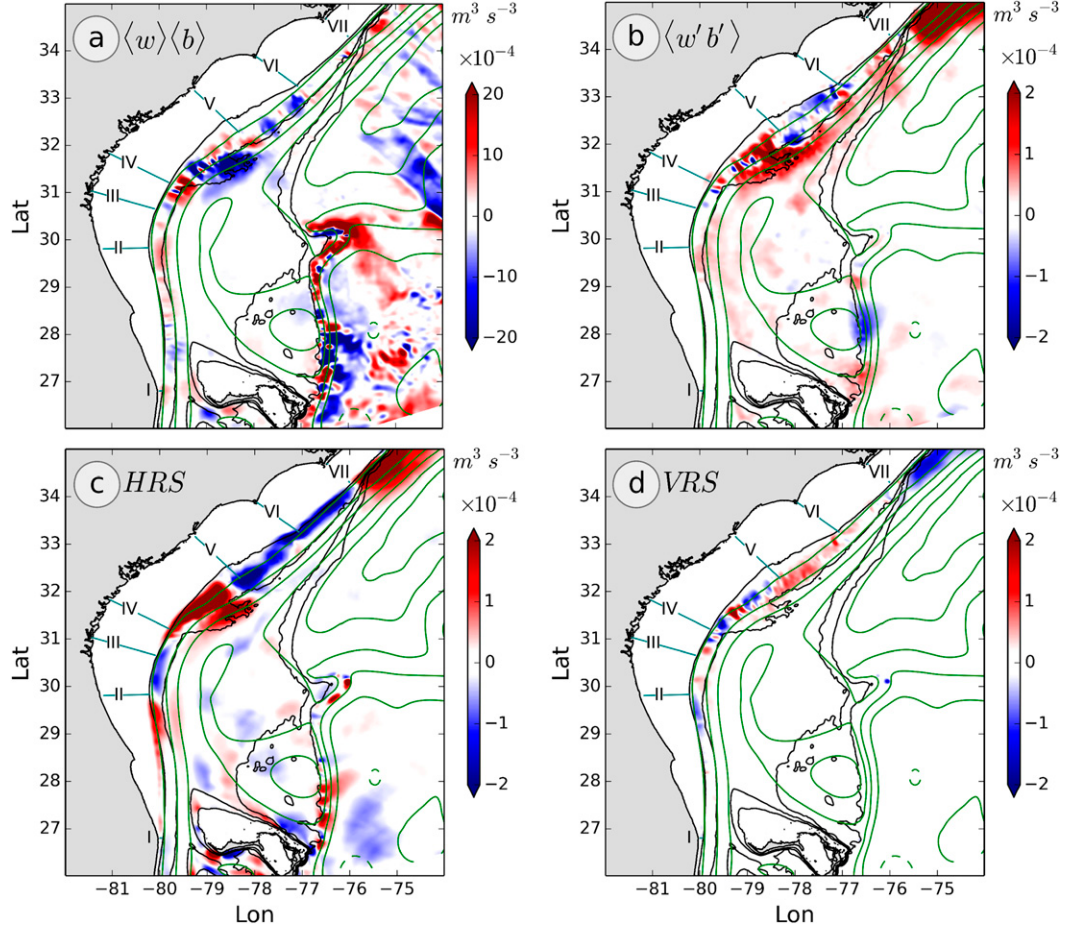


FIG. 16. Depth-integrated (a)  $P_m K_m = \langle w \rangle \langle b \rangle$ , (b)  $P_e K_e = \langle w'b' \rangle$ , (c) HRS, and (d) VRS for ROMS2 ( $\text{m}^3 \text{s}^{-3}$ ). Note that the scale of (a) is 10 times larger than the scale of the other panels. All fields have been horizontally smoothed using a convolution with a Gaussian kernel of half-width 10 km. Topography is shown in black contours at 0-, 200-, 600-, 1000-, and 2000-m isobaths. Barotropic streamfunction is shown in green with a 10-Sv interval.

The instabilities that arise when  $fq < 0$ , where  $q$  is Ertel's potential vorticity, also extract kinetic energy through a combination of  $\langle w'b' \rangle$ , HRS, and VRS (Thomas et al. 2013). Inertial (or centrifugal) instability is triggered when the relative vorticity is smaller than  $-f$  and extracts its energy mostly from the lateral shear ( $\text{HRS} > 0$ ). The intense negative vorticity generation along the Bahamas slope (Fig. 7a) and the positive conversion due to HRS seen at  $26^\circ\text{N}, 79.5^\circ\text{W}$  and  $27.5^\circ\text{N}, 79.5^\circ\text{W}$  in Fig. 16c are indicative of such inertial instability.

Along-stream variations of eddy kinetic energy  $\text{EKE} = 0.5(\langle u^2 \rangle + \langle v^2 \rangle)$  and the two source terms HRS and  $\langle w'b' \rangle$  are shown in Fig. 17. These quantities have been integrated vertically over the entire water column and in the cross-stream direction over the full stream and multiplied by the mean density  $\rho_0 = 1027.4 \text{ kg m}^{-3}$  such that the unit of EKE is Joules per meter, and the unit of the eddy conversion terms is Joules per meter per second. The variations of EKE along the stream show

a weak growth of eddy energy upstream of the bump, a rapid growth at the Charleston Bump, a decay downstream of the bump, and again a large increase past Cape Lookout. This is consistent with the patterns of the energy conversions terms whose sum is weakly positive upstream of the bump, strongly positive at the bump, negative downstream of the bump, and again strongly positive past Cape Lookout. Amplitudes of the baroclinic and barotropic energy conversions and their overall contribution to the EKE variations are comparable. The barotropic signal is larger than the baroclinic after the Florida Straits and at the bump, but the baroclinic signal is slightly larger downstream of Cape Lookout.

The variations of EKE and the energy conversions terms are in agreement with the observations of variability around the bump and off Onslow Bay described in Olson et al. (1983) and Dewar and Bane (1985). However, observational results point to a positive baroclinic conversion and a negative barotropic conversion

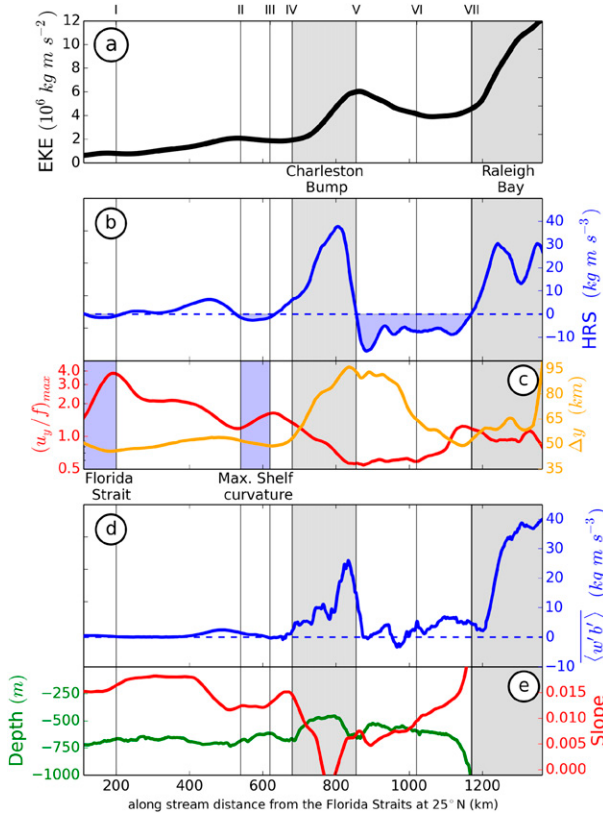


FIG. 17. Along-stream (a) EKE (black), (b) barotropic HRS energy conversion term (blue), (c) maximum cross-stream gradient of along-stream velocity  $u_y/f$  (red) and horizontal cross-stream distance  $\Delta y$  (orange) between the center of the stream (defined as the  $\Psi = 11\text{-Sv}$  streamfunction contour) and the shelf (defined as the  $z = -50\text{-m}$  isobath), (d) baroclinic  $\langle w'b' \rangle$  (blue) energy conversion term, and (e) depth of the bottom topography at the center of the stream (green) and mean topographic slope (red) between the center of the stream and its inshore front (defined as the  $\Psi = 11\text{-Sv}$  and  $\Psi = 1\text{-Sv}$  streamfunction contours, respectively). The along-stream direction is chosen as the barotropic streamfunction contour  $\Psi = 1\text{ Sv}$  (see Fig. 16), and the along-stream distance is computed from the boundary of the ROMS2 domain in the Florida Strait at ( $25^\circ \text{N}$ ,  $79.8^\circ \text{W}$ ). The terms  $u$ ,  $v$  are the velocities along the local coordinates  $(x, y)$  defined as along- and cross-stream directions, respectively. Locations of the Charleston Bump and Raleigh Bay correspond to the filled gray areas. The thin black vertical lines indicate the positions of the sections plotted in Fig. 16.

off Raleigh Bay (Savidge and Bane 2004), whereas the model indicates strong positive baroclinic and barotropic conversions. The difference is partially explained because Savidge and Bane (2004) computed energy conversion terms at 300-m depth, whereas a significant part of the energy conversion in the model is due to the variability in the lower water column ( $z < -400\text{ m}$ ) where the deep western boundary current is crossing below the Gulf Stream. The barotropic energy conversion term integrated over the upper ocean only ( $z > -400\text{ m}$ , not shown) is weaker in amplitude and

more spatially contrasted with regions of positive and negative signals.

The pattern of the kinetic energy conversion and the meandering growth or decay is interpreted in Dewar and Bane (1985) as primarily because of the topographic constraint. To further understand how the topography influences the stability of the flow and eddy generation, we look at the correlations of the along-stream variations of different quantities related to the geometry of the continental slope with eddy kinetic energy and energy conversion term variations.

The baroclinic source term  $\langle w'b' \rangle$  is associated with the vertical shear in the flow and is very sensitive to the shape of the bottom topography. The depth of the bottom topography at the center of the stream and the mean topographic slope between the center of the stream and the shelf (defined as the  $\Psi = 11\text{-Sv}$  and  $\Psi = 1\text{-Sv}$  streamfunction contours, respectively) are shown in Fig. 17. The correlation between the slope variations and  $\langle w'b' \rangle$  clearly points to a local topographic stabilization interpretation.

The continental slope does not vary much between the Florida Strait and Charleston Bump, as seen previously from Figs. 7a and 7b, with values between  $s = 0.01$  and  $s = 0.02$ . The slightly positive ratio between the slopes of the topography and the isotherms corresponds to a moderate stabilization of the flow. The first local maxima for the baroclinic source term at  $x = 500\text{ km}$  (between  $29^\circ$  and  $30^\circ \text{N}$  in Fig. 16) coincide with local minima in the slope. The large increase of  $\langle w'b' \rangle$  corresponds to the region where the stream is disrupted and loses contact with the slope (Fig. 7c). The mean slope felt by the flow decreases toward very small values and allows the flow to become strongly baroclinically unstable. Between the Charleston Bump and Cape Hatteras the slope of the topography gradually increases and  $\langle w'b' \rangle$  decreases accordingly. Right after the bump the ratio between the topography slope and isotherms is close to 1 (Fig. 7d), leading to a strong stabilization of the flow. The slope becomes steeper downstream and almost vertical at Cape Lookout, as shown by Fig. 7f, leading to another outburst of instability.

The use of linear stability results to interpret local instabilities of the flow can usually be made under the assumption that the slope variations in the along-stream direction occur on a scale large relative to the wavelength of the unstable modes. This is not the case here as the scale of the meanders is often similar to the scale of the along-stream variations of topography (Fig. 1). Topographic variations at the bump form a gap with a limited extent ( $L \approx 100\text{ km}$ ) where the flow is unstable, while the slope is stabilizing the flow upstream and downstream of this gap. Samelson and Pedlosky (1990)

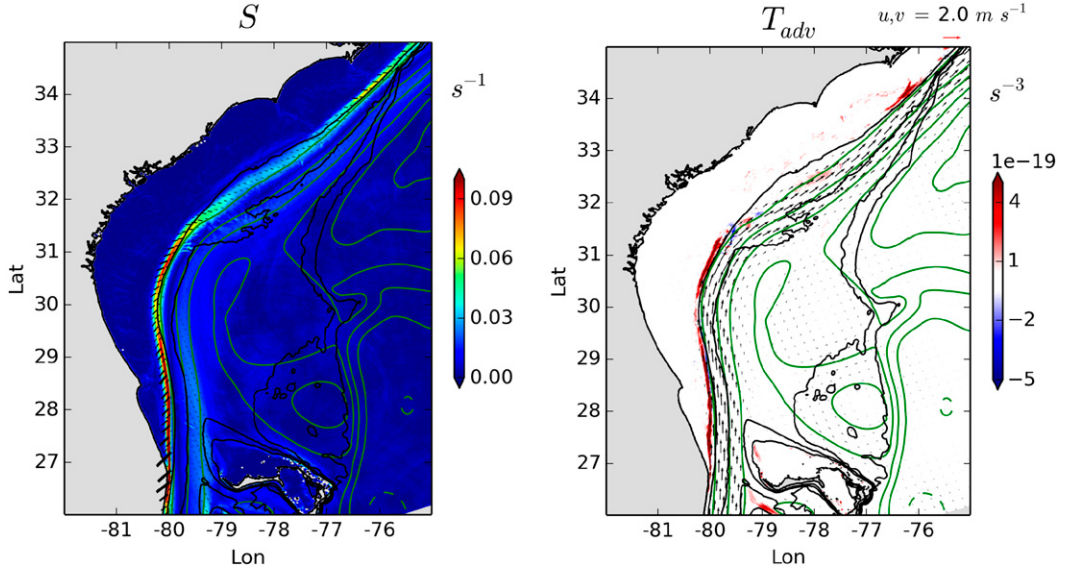


FIG. 18. (left) Mean strain rate (colors) and principal strain axis (black lines), and (right) frontal tendency due to horizontal advection  $T_{adv}$  (colors) and surface velocity (arrows) for ROMS2. Topography is shown in black contours at 0-, 200-, 600-, 1000-, and 2000-m isobaths. Barotropic streamfunction is shown in green with a 10-Sv interval.

studied such a configuration in a two-layer QG model and showed that baroclinic instability can grow locally even when the unstable region has a limited extent, comparable or smaller than the wavelengths of unstable modes. Growth rates become small only for intervals shorter than the Rossby deformation radius. The analysis in Samelson and Pedlosky (1990) shows that the unstable modes are trapped in the gap; they grow in time but decay in space downstream of the unstable region such that the maximum mode amplitudes occur near the downstream edge of the unstable interval. This explains the location of the EKE local maximum in Fig. 17 at the tail of the bump.

The impact of topography is not as straightforward for barotropic instability mechanisms. There are different competing nonlinear effects due to the topography. On one hand, the slope acts to sharpen the cross-stream velocity and vorticity gradients (see section 3) and therefore increases growth rates of a barotropic shear-type instability. On the other hand, the topography also acts to inhibit the eddy activity by increasing straining and limiting the cross-stream growth of the meanders.

The along-stream variations for the maximum cross-stream gradient of along-stream velocity  $u_y/f$ , which is the only contributing term in the shear ( $v_x + u_y$ ) and horizontal strain [ $S = \sqrt{(u_x - v_y)^2 + (v_x + u_y)^2}$ ], are shown in Fig. 17c. The shear increases when the flow presses against the shelf because of a combination of bathymetric curvature and inertia effects. Variations of

the shear match perfectly the variations of the inverse of the horizontal cross-stream distance between the center of the stream (defined as the  $\Psi = 11$ -Sv streamfunction contour) and the shelf (defined as the  $z = -50$ -m isobath) shown in Fig. 17c. The shear is at its maximum at the exit of the Straits of Florida ( $27^{\circ}\text{N}$ ), where the stream is strongly squeezed against the shelf because of the narrow channel formed by the topography (Fig. 7a). There is a second maximum upstream of the Charleston Bump at about  $30.5^{\circ}\text{N}$ , where the curvature of the bathymetry toward the northeast is at its maximum. The curvature locally peaks at  $0.004\text{ km}^{-1}$ , corresponding to a small radius of curvature of 250 km. Finally, the third shear maximum is visible upstream of Cape Lookout after the stream has recovered from the bump's seaward deflection and is again pressed against the slope. These three locations correspond to local minima of HRS and precede increases of HRS and corresponding outbursts of barotropic shear instability. HRS is anticorrelated with the derivative of the shear such that meanders grow when the shear is decreasing, and meander growth is suppressed when the shear is increasing.

The mean strain rate and advective frontal tendency at the surface are shown in Fig. 18. The frontal tendency shows how efficient the straining is at sharpening the buoyancy gradients on the cyclonic side of the Gulf Stream. The eddy decay regions are the regions associated with elongation of frontal features.

It should be noted that the second peak of HRS starts right after the bathymetric curvature maximum, as shown in Fig. 17, before arriving at the Charleston

Bump, and is then strongly amplified when passing the bump. This confirms that both the bathymetric curvature and the Charleston Bump play a role in the eddy generation along the shelf, as was shown by Xie et al. (2007), using simulations with idealized topography profiles. The bathymetric curvature constantly controls the variations of the barotropic energy conversion term, and the Charleston Bump acts to locally increase both barotropic and baroclinic energy conversion terms.

The patterns of HRS are better explained by looking at the life cycles of eddies that grow through barotropic shear instability and subsequently decay. Eddy generation originates from the mean velocity shear and is acting to reduce it. By analogy with an atmospheric storm track, there is eddy growth by Reynolds stress and downstream development of the eddies (Williams et al. 2007). Interaction of the flow with the topography acts as an external forcing process to localize these oceanic storm tracks by sharpening the cyclonic side of the stream at the three above-mentioned locations. Regions of negative barotropic conversion are regions of eddy decay. Eddies are tilted with the increasing background shear and return energy and momentum to the mean flow following the Orr mechanism (Orr 1907). Eddy growth provides a deceleration of the mean flow in the region of positive HRS, and eddy decay provides an acceleration of the flow in the region of negative HRS.

### b. Eddy fluxes

In section 5a, we have seen that eddies were acting to reshape the mean currents with strong downgradient eddy momentum fluxes ( $HRS > 0$ ) in the Charleston Bump region and upgradient eddy momentum fluxes ( $HRS < 0$ ) between the bump and Cape Lookout. We investigate here eddy fluxes of buoyancy and other dynamical quantities, their impact on the mean flow, and the possibility of cross-shelf exchanges between the flow and the shelf.

The depth-integrated time-mean eddy fluxes of buoyancy  $b$ , relative vorticity  $\zeta$ , and Ertel potential vorticity [PV;  $q = (f\mathbf{z} + \nabla \times \mathbf{u}) \cdot \nabla b$ ] are shown Fig. 19 in the along-stream and cross-stream directions. The along-stream direction is defined as parallel to the barotropic streamfunction contour  $\Psi = 1$  Sv. Using a different barotropic streamfunction contour as a reference does not change the following results in any important ways. The terms  $u, v$  are the velocities along the local coordinates  $(x, y)$  defined as along- and cross-stream directions, respectively. The value of  $x$  is positive in the direction of the flow, and  $y$  is oriented from the flow to the coast so that a positive cross-stream flux corresponds to a flux from the Gulf Stream to the shelf. Perturbations relative to the time

mean are denoted with a prime such that any variable can be written  $u = \langle u \rangle + u'$ , and so on. Integration over the total depth of the flow is denoted by an overbar. We do not show here the corresponding vertical fluxes, which are negligible. Vertical fluxes of buoyancy, which have been shown in Fig. 16c, are important in the energy equation but not for the buoyancy budget. The vertical divergence of vertical eddy buoyancy fluxes is several orders of magnitude smaller than the divergence of the horizontal eddy fluxes.

All eddy fluxes have significant alongshore variations, in particular at the northern limit of the Charleston Bump, where the Reynolds stress HRS changes sign (Fig. 16b). We define two different stream sectors (dashed lines in Fig. 19): sector A corresponds to an eddy growth region and covers the Charleston Bump area, and sector B corresponds to an eddy decay region and starts downstream of the bump and extends to Cape Lookout. Vertical sections of the cross-stream eddy fluxes  $\langle v'b' \rangle$ ,  $\langle v'\zeta' \rangle$ , and  $\langle v'q' \rangle$  averaged in the along-stream direction over these two different sectors are shown in Fig. 20. In sector A, over the Charleston Bump, eddy vorticity fluxes are positive on the inshore side, negative in the center of the stream, and slightly positive on the offshore side. They are convergent at the location of the mean relative vorticity minimum and divergent at the location of the mean relative vorticity maximum. They act in the sense of an eddy flux down the mean gradient with respect to  $\partial\langle\zeta\rangle/\partial y$ . This is consistent with the strong generation of eddies in this region by the mean flow that acts to weaken the velocity shear and relative vorticity of the mean flow (section 3). In sector B, downstream of the bump, signs are reversed such that eddy vorticity fluxes are negative on the inshore side and positive on the offshore side, showing that mean velocity gradients are now reinforced by the eddies.

Eddy buoyancy fluxes are also downgradient in sector A over the Charleston Bump. There are large positive fluxes inshore and negative fluxes offshore. These fluxes are limiting isopycnal slopes in the interior and acting toward a restratification of the flow. Because salinity plays a relatively minor role compared to temperature in the buoyancy distribution and nonlinear effects in the equation of state are not qualitatively important, heat and temperature are closely related to buoyancy. Eddies are fluxing heat out of the Gulf Stream in this region. In sector B, there are still negative eddy buoyancy fluxes on the offshore side, but there are no more positive fluxes on the inshore side except in a thin ( $\approx 50$  m) surface layer. Eddy buoyancy fluxes are negative and upgradient in the vicinity of the slope, acting to increase the lateral buoyancy gradients on the inshore side of the stream.

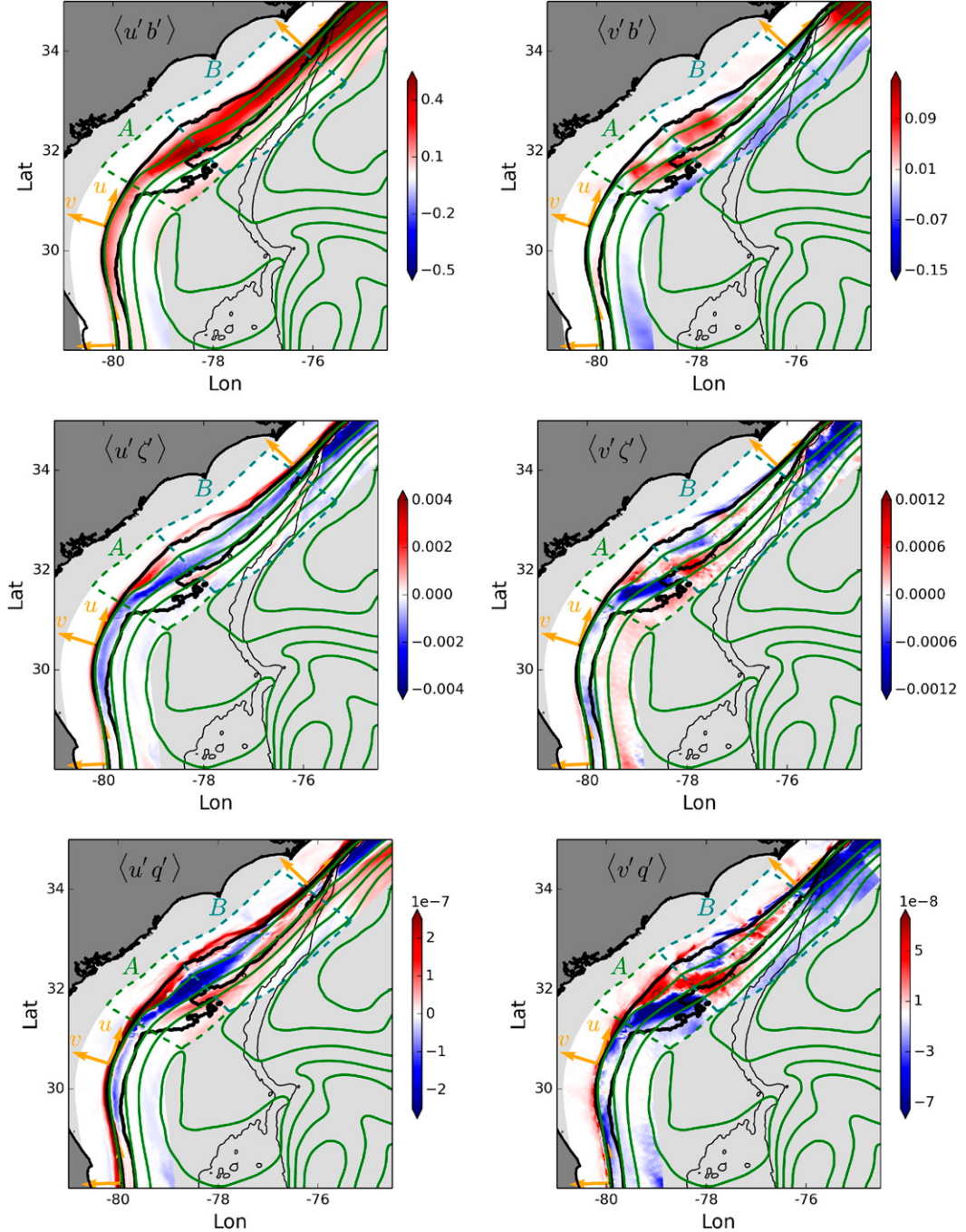


FIG. 19. Depth-integrated time-mean eddy fluxes of (top) buoyancy ( $\text{m}^3 \text{s}^{-3}$ ), (middle) relative vorticity ( $\text{m}^2 \text{s}^{-2}$ ), and (bottom) potential vorticity ( $\text{m}^2 \text{s}^{-4}$ ) in the (left) along-stream direction and in the (right) cross-stream direction for ROMS2. The along-stream direction is chosen as the barotropic streamfunction contour  $\Psi = 1 \text{ Sv}$ . The terms  $u, v$  are the velocities along the local coordinates ( $x, y$ ) defined as along- and cross-stream directions, respectively. The value  $x$  is positive in the direction of the flow, and  $y$  is oriented from the flow to the coast so that a positive cross-stream flux corresponds to a flux from the Gulf Stream to the shelf. Barotropic streamfunction is shown in green with a 10-Sv interval.

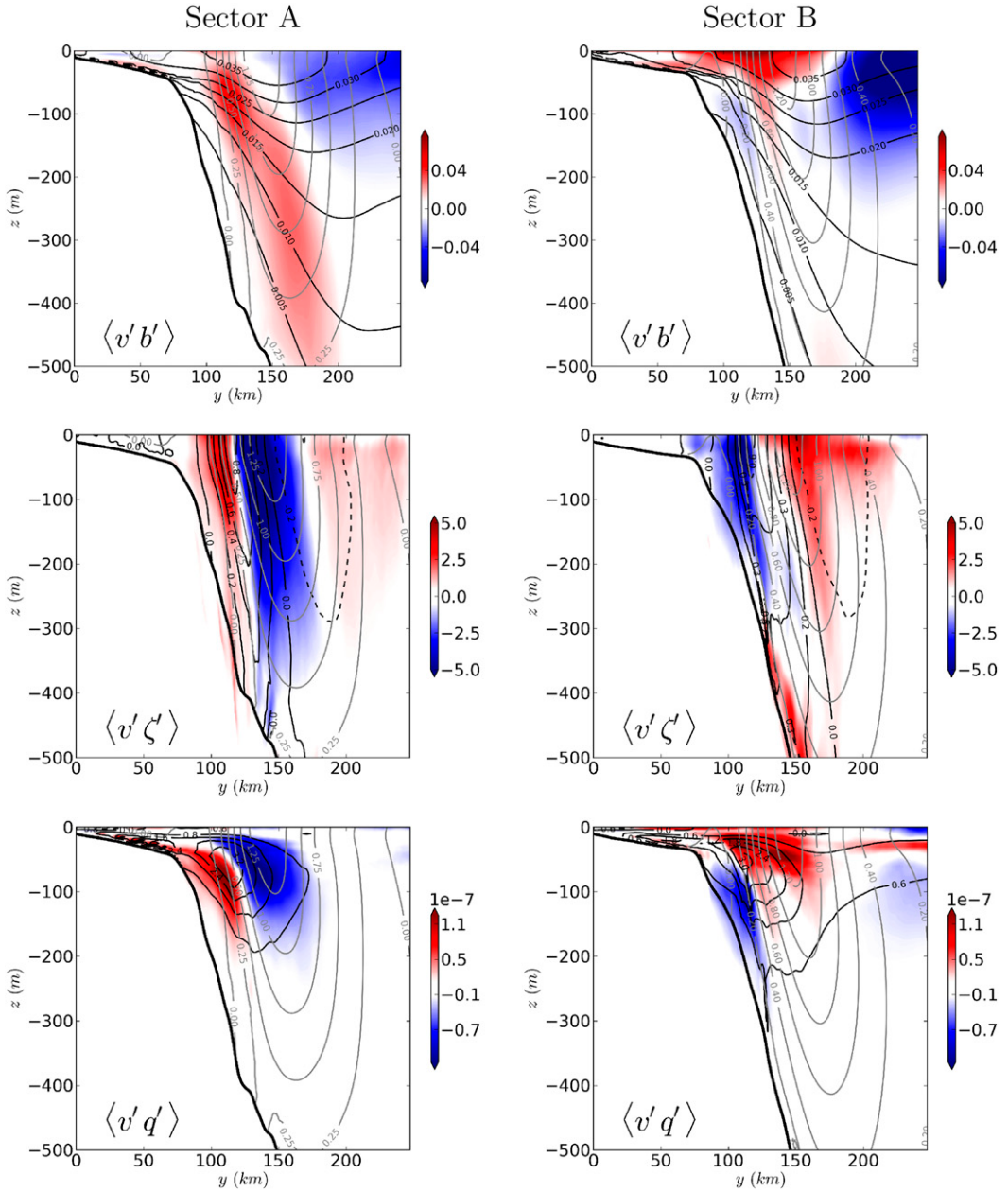


FIG. 20. Vertical sections of time-mean cross-stream eddy fluxes integrated in the along-stream direction for (top) buoyancy ( $\langle v' b' \rangle$ ;  $\text{m}^3 \text{s}^{-3}$ ), (middle) relative vorticity ( $\langle v' \zeta' \rangle$ ;  $\text{m}^2 \text{s}^{-2}$ ), and (bottom) PV ( $\langle v' q' \rangle$ ;  $\text{m}^2 \text{s}^{-4}$ ) for ROMS2. Black contours show the mean profiles of  $b$ ,  $\zeta$ , and  $q$ . Gray contours show the mean along-stream velocity. Left panels correspond to the Charleston Bump area (sector A in Fig. 19) and right panels correspond to the area between the bump and Cape Lookout (sector B in Fig. 19). The thick black line indicates the mean position of the bathymetry.

Eddy fluxes of PV are only significant in the upper 200 m of the flow, where the larger amplitude of the PV gradients occur (Fig. 20). Eddy fluxes are downgradient with respect to  $\partial_y(q)$  in sector A. Positive eddy fluxes inshore and negative fluxes offshore are acting to flux PV out of the Gulf Stream and weaken the PV maximum at the North Wall. Signs are reversed in sector B

with negative fluxes inshore along the shelf between  $z = -100$  m and  $z = -220$  m, corresponding mostly to the creation of positive PV due to the effect of the turbulent bottom drag along the slope.

For all variables computed, eddy growth/decay regions are associated with downgradient/upgradient eddy fluxes, respectively. This follows Wilson and Williams

(2006) who find that eddy tracer fluxes are directed downgradient when there is a Lagrangian increase in tracer variance or a dissipation of tracer variance. For small tracer dissipation, the effect of eddies depends on whether the eddies are locally growing or decaying. In the present configuration, eddy growth and decay regions are locked by topographic features such that there is a systematic effect of eddies in these regions.

## 6. Summary and conclusions

The Gulf Stream strongly interacts with the topography along the southeast U.S. continental boundary between the Straits of Florida and Cape Hatteras. The dynamics of the Gulf Stream in this region is investigated with a set of realistic, very high-resolution simulations (from  $\Delta x = 2.5$  km to  $\Delta x = 750$  m) using the oceanic model ROMS. Validation of the characteristics of the flow in the simulation, including its path, velocity, transport, vertical structure, and variability is achieved through comparison with available satellite and in situ observations.

The mean path of the flow is strongly influenced by the topography and in particular by the interactions with the Charleston Bump. There is significant local topographic form drag and bottom pressure torque exerted by the bump that retard the mean flow and steer the mean current pathway seaward. The high positive bottom pressure on the upstream side of the bump is forcing the current above and around the bump and changing its mean direction to locally eastward. The smaller amplitude but wider negative bottom pressure on the downstream side allows the current to progressively change back its direction to northward. The topographic impact of the shelf more generally provides, through bottom pressure torque, the positive input of barotropic vorticity necessary to balance the meridional transport of the planetary vorticity gradient and help close the gyre-scale vorticity balance.

The effect of the topography on the development and evolution of meanders and eddies is studied by computing energy budgets of the eddies and the mean flow. Eddy kinetic energy (EKE) is steadily growing between the Florida Straits and the bump, growing rapidly at the bump, decaying downstream of the bump, and again greatly increasing past Cape Lookout, in agreement with past observations. Barotropic energy conversion through horizontal Reynolds stress and baroclinic conversion through vertical eddy fluxes of buoyancy are both contributing to the along-stream variations of EKE.

The baroclinic instability is stabilized by the cross-stream slope everywhere but at the Charleston Bump. The observed meander growth on the inshore side of the

stream upstream of the bump is due primarily to barotropic shear instability. Very strong cyclonic shear values precede the regions of positive barotropic conversion. Eddies are generated between the exit of the Straits of Florida and the point of maximum bathymetric curvature where the flow is squeezed against the slope. The combination of topographic curvature and flow inertia create large straining values and positive frontal tendencies that restrict meander growth and increase the horizontal shear of the mean flow. The topographic constraint is reduced past the Charleston Bump as the stream moves seaward and the flow is allowed to become strongly unstable through a mixed barotropic–baroclinic instability process. As a result, the amplitudes of the meanders rapidly increase as they progress northeastward. The continental slope steepens and stabilizes baroclinic instability again downstream of the Charleston Bump. Meander energy is converted back into mean energy, a process that results in decreasing meander amplitudes and reinforcement of the shear of the mean flow. The topographic constraint is relieved again off of Cape Lookout as the slope becomes almost vertical and both barotropic and baroclinic mean-to-eddy energy conversions increase.

The patterns of the horizontal Reynolds stress are well explained by looking at the life cycle of eddies, their generation, and downstream development. By analogy with an atmospheric storm track, eddies grow through barotropic shear instability and subsequently decay. Interactions of the flow with the topography act as external forcing processes to localize these oceanic storm tracks.

Associated time-averaged eddy fluxes are essential to maintain and reshape the mean current. Eddy fluxes of momentum are acting to decelerate the stream in the unstable regions, after the exit of the Straits of Florida and at the Charleston Bump, and accelerate it in stable regions in between, especially between the bump and Cape Lookout. The eddy fluxes of vorticity, buoyancy, and PV are also downgradient in the Charleston Bump area and revert to upgradient in the area between the bump and Cape Lookout. The pattern of eddy fluxes is explained in terms of eddy life cycle. Eddy growth regions are associated with downgradient eddy fluxes and eddy decay regions with upgradient eddy fluxes.

**Acknowledgments.** We appreciate support from the Office of Naval Research (N00014-12-1-0939 and N00014-12-1-0105) and the National Science Foundation (OCE-1049134). The Explorer of the Seas ADCP dataset was produced by the Rosenstiel School of Marine and Atmospheric Science, with support from SEACOOS and NOAA. Data were processed and provided by Lisa

Beal, Liz Williams, and Warner Baringer. The altimeter products were produced by Ssalto/Duacs and distributed by AVISO, with support from CNES ([www.aviso.altimetry.fr/duacs/](http://www.aviso.altimetry.fr/duacs/)). We also thank an anonymous reviewer for constructive feedback in revising the manuscript.

## REFERENCES

- Bane, J., Jr., and W. Dewar, 1988: Gulf Stream bimodality and variability downstream of the Charleston Bump. *J. Geophys. Res.*, **93**, 6695–6710, doi:[10.1029/JC093iC06p06695](https://doi.org/10.1029/JC093iC06p06695).
- Barnier, B., L. Siefried, and P. Marchesiello, 1995: Thermal forcing for a global ocean circulation model using a three-year climatology of ECMWF analyses. *J. Mar. Syst.*, **6**, 363–380, doi:[10.1016/0924-7963\(94\)00034-9](https://doi.org/10.1016/0924-7963(94)00034-9).
- Beal, L., J. Hummon, E. Williams, O. Brown, W. Baringer, and E. Kearns, 2008: Five years of Florida Current structure and transport from the Royal Caribbean Cruise Ship *Explorer of the Seas*. *J. Geophys. Res.*, **113**, C06001, doi:[10.1029/2007JC004154](https://doi.org/10.1029/2007JC004154).
- Beckmann, A., and D. Haidvogel, 1993: Numerical simulation of flow around a tall isolated seamount. Part I: Problem formulation and model accuracy. *J. Phys. Oceanogr.*, **23**, 1736–1753, doi:[10.1175/1520-0485\(1993\)023<1736:NSOFAA>2.0.CO;2](https://doi.org/10.1175/1520-0485(1993)023<1736:NSOFAA>2.0.CO;2).
- Blanton, J., L. Atkinson, L. Pietrafesa, and T. Lee, 1981: The intrusion of Gulf Stream water across the continental shelf due to topographically-induced upwelling. *Deep-Sea Res.*, **28**, 393–405, doi:[10.1016/0198-0149\(81\)90006-6](https://doi.org/10.1016/0198-0149(81)90006-6).
- Boccaletti, G., R. Ferrari, and B. Fox-Kemper, 2007: Mixed layer instabilities and restratification. *J. Phys. Oceanogr.*, **37**, 2228–2250, doi:[10.1175/JPO3101.1](https://doi.org/10.1175/JPO3101.1).
- Carton, J., and B. Giese, 2008: A reanalysis of ocean climate using Simple Ocean Data Assimilation (SODA). *Mon. Wea. Rev.*, **136**, 2999–3017, doi:[10.1175/2007MWR1978.1](https://doi.org/10.1175/2007MWR1978.1).
- Conkright, M., R. Locarnini, H. Garcia, T. O'Brien, T. Boyer, C. Stephens, and J. Antonov, 2002: *World Ocean Atlas 2001: Objective Analyses, Data Statistics and Figures*. National Oceanographic Center Internal Tech. Rep. 17, CD-ROM.
- Dewar, W., and J. Bane Jr., 1985: Subsurface energetics of the Gulf Stream near the Charleston Bump. *J. Phys. Oceanogr.*, **15**, 1771–1789, doi:[10.1175/1520-0485\(1985\)015<1771:SEOTGS>2.0.CO;2](https://doi.org/10.1175/1520-0485(1985)015<1771:SEOTGS>2.0.CO;2).
- Ducet, N., and P.-Y. Le Traon, 2001: A comparison of surface eddy kinetic energy and Reynolds stresses in the Gulf Stream and the Kuroshio current systems from merged TOPEX/Poseidon and ERS-1/2 altimetric data. *J. Geophys. Res.*, **106**, 16 603–16 622, doi:[10.1029/2000JC000205](https://doi.org/10.1029/2000JC000205).
- Glenn, S., and C. Ebbesmeyer, 1994: The structure and propagation of a Gulf Stream frontal eddy along the North Carolina shelf break. *J. Geophys. Res.*, **99**, 5029–5046, doi:[10.1029/93JC02786](https://doi.org/10.1029/93JC02786).
- Gula, J., and V. Zeitlin, 2014: Instabilities of shallow-water flows with vertical shear in the rotating annulus. *Modelling Atmospheric and Oceanic Flows: Insights from Laboratory Experiments and Numerical Simulations*, T. von Larcher and P. Williams, Eds., Amer. Geophys. Union, 119–138.
- , M. Molemaker, and J. McWilliams, 2014: Submesoscale cold filaments in the Gulf Stream. *J. Phys. Oceanogr.*, **44**, 2617–2643, doi:[10.1175/JPO-D-14-0029.1](https://doi.org/10.1175/JPO-D-14-0029.1).
- Hood, C., and J. Bane Jr., 1983: Subsurface energetics of the Gulf Stream cyclonic frontal zone off Onslow Bay, North Carolina. *J. Geophys. Res.*, **88**, 4651–4662, doi:[10.1029/JC088iC08p04651](https://doi.org/10.1029/JC088iC08p04651).
- Hughes, C., 2000: A theoretical reason to expect inviscid western boundary currents in realistic oceans. *Ocean Modell.*, **2**, 73–83, doi:[10.1016/S1463-5003\(00\)00011-1](https://doi.org/10.1016/S1463-5003(00)00011-1).
- , and B. De Cuevas, 2001: Why western boundary currents in realistic oceans are inviscid: A link between form stress and bottom pressure torques. *J. Phys. Oceanogr.*, **31**, 2871–2886, doi:[10.1175/1520-0485\(2001\)031<2871:WWBCIR>2.0.CO;2](https://doi.org/10.1175/1520-0485(2001)031<2871:WWBCIR>2.0.CO;2).
- Jackson, L., C. Hughes, and R. Williams, 2006: Topographic control of basin and channel flows: The role of bottom pressure torques and friction. *J. Phys. Oceanogr.*, **36**, 1786–1805, doi:[10.1175/JPO2936.1](https://doi.org/10.1175/JPO2936.1).
- Large, W., J. McWilliams, and S. Doney, 1994: Oceanic vertical mixing: A review and a model with a nonlocal boundary layer parameterization. *Rev. Geophys.*, **32**, 363–403, doi:[10.1029/94RG01872](https://doi.org/10.1029/94RG01872).
- Leaman, K., E. Johns, and T. Rossby, 1975: The average distribution of volume transport and potential vorticity with temperature at three sections across the Gulf Stream. *J. Geophys. Res.*, **80**, 1975–1978, doi:[10.1029/JC080i015p01975](https://doi.org/10.1029/JC080i015p01975).
- Lee, T., and L. Atkinson, 1983: Low-frequency current and temperature variability from Gulf Stream frontal eddies and atmospheric forcing along the southeast U.S. outer continental shelf. *J. Geophys. Res.*, **88**, 4541–4567, doi:[10.1029/JC088iC08p04541](https://doi.org/10.1029/JC088iC08p04541).
- , J. Yoder, and L. Atkinson, 1991: Gulf Stream frontal eddy influence on productivity of the southeast U.S. continental shelf. *J. Geophys. Res.*, **96**, 22 191–22 205, doi:[10.1029/91JC02450](https://doi.org/10.1029/91JC02450).
- Lemarié, F., J. Kurian, A. Shchepetkin, M. Molemaker, F. Colas, and J. McWilliams, 2012: Are there inescapable issues prohibiting the use of terrain-following coordinates in climate models? *Ocean Modell.*, **42**, 57–79, doi:[10.1016/j.ocemod.2011.11.007](https://doi.org/10.1016/j.ocemod.2011.11.007).
- Lin, G., and J. Atkinson, 2000: A mechanism for offshore transport across the Gulf Stream. *J. Phys. Oceanogr.*, **30**, 225–232, doi:[10.1175/1520-0485\(2000\)030<0225:AMFOTA>2.0.CO;2](https://doi.org/10.1175/1520-0485(2000)030<0225:AMFOTA>2.0.CO;2).
- Locarnini, R. A., and Coauthors, 2013: *Temperature*. Vol. 1, *World Ocean Atlas 2013*, NOAA Atlas NESDIS 73, 40 pp.
- Marchesiello, P., J. McWilliams, and A. Shchepetkin, 2001: Open boundary conditions for long-term integration of regional oceanic models. *Ocean Modell.*, **3**, 1–20, doi:[10.1016/S1463-5003\(00\)00013-5](https://doi.org/10.1016/S1463-5003(00)00013-5).
- Mason, E., M. Molemaker, A. Shchepetkin, F. Colas, J. McWilliams, and P. Sangra, 2010: Procedures for offline grid nesting in regional ocean models. *Ocean Modell.*, **35**, 1–15, doi:[10.1016/j.ocemod.2010.05.007](https://doi.org/10.1016/j.ocemod.2010.05.007).
- McClain, C., and L. Atkinson, 1985: A note on the Charleston Gyre. *J. Geophys. Res.*, **90**, 11 857–11 861, doi:[10.1029/JC090iC06p11857](https://doi.org/10.1029/JC090iC06p11857).
- , L. Pietrafesa, and J. Yoder, 1984: Observations of Gulf Stream-induced and wind-driven upwelling in the Georgia Bight using ocean color and infrared imagery. *J. Geophys. Res.*, **89**, 3705–3723, doi:[10.1029/JC089iC03p03705](https://doi.org/10.1029/JC089iC03p03705).
- McWilliams, J., 2008: The nature and consequences of oceanic eddies. *Ocean Modeling in an Eddying Regime*, *Geophys. Monogr.*, Vol. 177, Amer. Geophys. Union, 5–15, doi:[10.1029/177GM03](https://doi.org/10.1029/177GM03).
- , E. Huckle, and A. Shchepetkin, 2009: Buoyancy effects in a stratified Ekman layer. *J. Phys. Oceanogr.*, **39**, 2581–2599, doi:[10.1175/2009JPO4130.1](https://doi.org/10.1175/2009JPO4130.1).
- Miller, J., and T. Lee, 1995: Gulf Stream meanders in the South Atlantic Bight: 1. Scaling and energetics. *J. Geophys. Res.*, **100**, 6687–6704, doi:[10.1029/94JC02542](https://doi.org/10.1029/94JC02542).
- Molemaker, J., J. McWilliams, and W. Dewar, 2015: Submesoscale instability and generation of mesoscale anticyclones near a separation of the California Undercurrent. *J. Phys. Oceanogr.*, doi:[10.1175/JPO-D-13-0225.1](https://doi.org/10.1175/JPO-D-13-0225.1), in press.

- Oey, L., 1988: A model of Gulf Stream frontal instabilities, meanders and eddies along the continental slope. *J. Phys. Oceanogr.*, **18**, 211–229, doi:10.1175/1520-0485(1988)018<0211:AMOGSF>2.0.CO;2.
- Olson, D., O. Brown, and S. Emmerson, 1983: Gulf Stream frontal statistics from Florida Straits to Cape Hatteras derived from satellite and historical data. *J. Geophys. Res.*, **88**, 4569–4577, doi:10.1029/JC088iC08p04569.
- Orlanski, I., 1969: The influence of bottom topography on the stability of jets in a baroclinic fluid. *J. Atmos. Sci.*, **26**, 1216–1233, doi:10.1175/1520-0469(1969)026<1216:TIOBTO>2.0.CO;2.
- Orr, W., 1907: The stability or instability of the steady motions of a perfect liquid and of a viscous liquid. *Proc. Roy. Ir. Acad.*, **27**, 69–138. [Available online at [www.jstor.org/stable/20490590](http://www.jstor.org/stable/20490590).]
- Pennel, R., A. Stegner, and K. Beranger, 2012: Shelf impact on buoyant coastal current instabilities. *J. Phys. Oceanogr.*, **42**, 39–61, doi:10.1175/JPO-D-11-016.1.
- Penven, P., L. Debreu, P. Marchesiello, and J. McWilliams, 2006: Application of the ROMS embedding procedure for the central California upwelling system. *Ocean Modell.*, **12**, 157–187, doi:10.1016/j.ocemod.2005.05.002.
- Porta Mana, P., and L. Zanna, 2014: Toward a stochastic parameterization of ocean mesoscale eddies. *Ocean Modell.*, **79**, 1–20, doi:10.1016/j.ocemod.2014.04.002.
- Poulin, F., A. Stegner, M. Hernández-Arencibia, A. Marrero-Díaz, and P. Sangrà, 2014: Steep shelf stabilization of the coastal Bransfield Current: Linear stability analysis. *J. Phys. Oceanogr.*, **44**, 714–732, doi:10.1175/JPO-D-13-0158.1.
- Rio, M., S. Guinehut, and G. Larnicol, 2011: New CNES-CLS09 global mean dynamic topography computed from the combination of GRACE data, altimetry, and in situ measurements. *J. Geophys. Res.*, **116**, C07018, doi:10.1029/2010JC006505.
- Risien, C., and D. Chelton, 2008: A global climatology of surface wind and wind stress fields from eight years of QuikSCAT scatterometer data. *J. Phys. Oceanogr.*, **38**, 2379–2413, doi:10.1175/2008JPO3881.1.
- Samelson, R., and J. Pedlosky, 1990: Local baroclinic instability of flow over variable topography. *J. Fluid Mech.*, **221**, 411–436, doi:10.1017/S0022112090003615.
- Savidge, D., and J. Bane Jr., 1999: Cyclogenesis in the deep ocean beneath the Gulf Stream: 2. Dynamics. *J. Geophys. Res.*, **104**, 18 127–18 141, doi:10.1029/1999JC900131.
- , and —, 2004: Gulf Stream meander propagation past Cape Hatteras. *J. Phys. Oceanogr.*, **34**, 2073–2085, doi:10.1175/1520-0485(2004)034<2073:GSMP>2.0.CO;2.
- Shchepetkin, A., and J. McWilliams, 2005: The Regional Oceanic Modeling System (ROMS): A split-explicit, free-surface, topography-following-coordinate ocean model. *Ocean Modell.*, **9**, 347–404, doi:10.1016/j.ocemod.2004.08.002.
- , and —, 2008: Computational kernel algorithms for finescale, multiprocess, longtime oceanic simulations. *Handb. Numer. Anal.*, **14**, 121–183, doi:10.1016/S1570-8659(08)01202-0.
- , and —, 2011: Accurate Boussinesq modeling with a practical, “stiffened” equation of state. *Ocean Modell.*, **38**, 41–70, doi:10.1016/j.ocemod.2011.01.010.
- Silva, A. D., C. Young, and S. Levitus, 1994: *Algorithms and Procedures*. Vol. 1, *Atlas of Surface Marine Data 1994*, NOAA Atlas NESDIS 6, 74 pp.
- Smith, W., and D. Sandwell, 1997: Global seafloor topography from satellite altimetry and ship depth soundings. *Science*, **277**, 1957–1962, doi:10.1126/science.277.5334.1956.
- Song, Y., and D. Wright, 1998: A general pressure gradient formulation for ocean models. Part II: Energy, momentum, and bottom torque consistency. *Mon. Wea. Rev.*, **126**, 3231–3247, doi:10.1175/1520-0493(1998)126<3231:AGPGFF>2.0.CO;2.
- Thomas, L., J. Taylor, R. Ferrari, and T. Joyce, 2013: Symmetric instability in the Gulf Stream. *Deep-Sea Res.*, **91**, 96–110, doi:10.1016/j.dsr2.2013.02.025.
- von Arx, W., D. Bumpus, and W. Richardson, 1955: On the fine-structure of the Gulf Stream front. *Deep-Sea Res.*, **3**, 46–65, doi:10.1016/0146-6313(55)90035-6.
- Webster, F., 1961: A description of Gulf Stream meanders off Onslow Bay. *Deep-Sea Res.*, **8**, 130–143, doi:10.1016/0146-6313(61)90005-3.
- Williams, R., C. Wilson, and C. Hughes, 2007: Ocean and atmosphere storm tracks: The role of eddy vorticity forcing. *J. Phys. Oceanogr.*, **37**, 2267–2289, doi:10.1175/JPO3120.1.
- Wilson, C., and R. Williams, 2006: On divergent barotropic and inertial instability in zonal-mean flow profiles. *J. Phys. Oceanogr.*, **36**, 189–201, doi:10.1175/JPO2841.1.
- Xie, L., X. Liu, and L. Pietrafesa, 2007: Effect of bathymetric curvature on Gulf Stream instability in the vicinity of the Charleston Bump. *J. Phys. Oceanogr.*, **37**, 452–475, doi:10.1175/JPO2995.1.
- Xue, H., and G. Mellor, 1993: Instability of the Gulf Stream Front in the South Atlantic Bight. *J. Phys. Oceanogr.*, **23**, 2326–2350, doi:10.1175/1520-0485(1993)023<2326:IOTGSF>2.0.CO;2.
- Yoder, J., L. Atkinson, S. Bishop, J. Blanton, T. Lee, and L. Pietrafesa, 1985: Phytoplankton dynamics within Gulf Stream intrusions on the southeastern United States continental shelf during summer 1981. *Cont. Shelf Res.*, **4**, 611–635, doi:10.1016/0278-4343(85)90033-0.
- Zhang, R., and G. Vallis, 2007: The role of bottom vortex stretching on the path of the North Atlantic western boundary current and on the northern recirculation gyre. *J. Phys. Oceanogr.*, **37**, 2053–2080, doi:10.1175/JPO3102.1.